ABSTRACT

Title of Thesis: CHARACTERIZATION OF TWO-PHOTON ABSORPTION DETECTORS FOR APPLICATIONS IN HIGH-SPEED OPTICAL SYSTEMS

Degree candidate: Reza Salem

Degree and year: Master of Science, 2003

Thesis directed by: Professor Thomas E. Murphy
Department of Electrical and Computer Engineering

This thesis investigates the process of two-photon absorption in optical detectors. We begin by describing some concepts of nonlinear optics and considering two-photon absorption as a nonlinear effect. We next mention some applications of two-photon absorption in high-speed optical communication systems. We describe the complete experimental characterization of two-photon absorption in a silicon avalanche photodiode. Two-photon absorption sensitivity factors and polarization dependence are investigated both theoretically and experimentally. Finally we compare the results of the measurements with those obtained from a similar detector.

CHARACTERIZATION OF TWO-PHOTON ABSORPTION DETECTORS FOR APPLICATIONS IN HIGH-SPEED OPTICAL SYSTEMS

by

Reza Salem

Thesis submitted to the faculty of the Graduate School of the
University of Maryland, College Park in partial fulfillment
of the requirements for the degree of
Master of Science
2003

Advisory Committee:

Professor Thomas E. Murphy, Chair
Professor Reza Ghodssi
Professor Julius Goldhar

ACKNOWLEDGEMENTS

I would like to give special thanks to my advisor Professor Thomas Murphy, for his guidance, encouragement and support. Not only did he introduce me to the experimental techniques in optics, but he also showed me how to present my work more effectively and professionally. He spent a significant amount of time supervising this work and always had time for my questions. He is one of the best teachers I have ever seen in my life.

I want to thank the faculty members of the University of Maryland who were my teachers during these two years of graduate studies. I especially want to thank Professor Julius Goldhar and Professor Reza Ghodssi for agreeing to serve on my thesis committee.

Also, I would like to thank Paveen Apiratikul and Shuo-Yen Tseng for their help in this thesis.

I am so grateful to Suzanne for her help and support during the time I worked on this thesis. And finally, I want to thank my family, Hassan, Mansooreh and Mahsa, who encouraged me to travel abroad and attend the graduate program at the University of Maryland. Their love and support from thousands of miles away has always given me the energy to work.

CONTENTS

LIST OF TABLES

LIST OF FIGURES

1. INTRODUCTION

In the last three decades, there has been increased interest in the development of optical communication systems. Development of high capacity optical time division multiplexed (OTDM) systems [4] has been especially important in this area. It has been recognized that in order to construct high speed OTDM systems, employing all-optical techniques can be one of the best solutions. All-optical networks employ ultrafast nonlinear effects and are faster and simpler in principle than electronically controller optical networks. The idea of controlling light with light was proposed more than 20 years ago. As an example we can mention the idea of the ultrafast all-optical gate [5] based on nonlinear effects in $LiNbO_3$. In the past two decades different methods for all-optical communication systems have been developed most of which include optical nonlinear effects. Two-photon absorption as a nonlinear effect has been considered an attractive solution for several applications including all-optical switching or demultiplexing.

Linear absorption in a detector happens when one photon creates one electron-hole pair in the detector. In this case the resulting photocurrent is proportional to the incident optical power. But under certain conditions two photons may be absorbed in a detector generating

one electron-hole pair and in this case the photocurrent is proportional to the square of the optical power. This phenomenon is called two-photon absorption (TPA) and is considered a third-order optical nonlinearity in the material. This thesis is an experimental study on the different factors affecting the TPA process in a detector. The detector used in this experiment is a silicon avalanche photodiode.

In Chapter 2 we discuss the theory of the TPA process based on the third-order nonlinear susceptibility tensor. Also in this chapter we briefly explain some applications of the TPA process described in previous research.

Chapter 3 presents some experimental measurement of TPA in a silicon photodetector. In this chapter first we show the main experimental setup and explain different elements of this setup. The curves showing the TPA response of the detector are given in this chapter. Sensitivity of the detector to the spot-size of the light focused on the detector is discussed theoretically and experimentally in this chapter. One of the main concerns in this chapter is the nonuniform response of the surface of the detector which is discussed in detail.

In Chapter 4 we describe the polarization sensitivity of the TPA process. Experimental result of the polarization dependence for linearly and elliptically polarized light are given in this chapter. Also theoretical analyses for isotropic and anisotropic materials are given and discussed based on the experimental results.

Chapter 5 compares the APD detector used in this experiment with another silicon APD detector and summarizes the conclusion gained from this comparison.

2. THEORY AND APPLICATIONS

This chapter is intended to explain some fundamental concepts of nonlinear optics, specifically two-photon absorption (TPA), and give a brief review of the applications introduced for two-photon absorption.

Nonlinear optics has been discussed in several text books [1, 6, 7] and the theoretical discussion given in this chapter is just a brief background of those topics needed to understand the concept of two-photon absorption. Starting in Section 2.1 we will give a simple analysis of second and third harmonic generation, intensity dependent refractive index and the general case of third-order nonlinear polarization. In Section 2.2 we give a general treatment of nonlinear susceptibility in a medium which leads to defining the susceptibility tensor. Section 2.3 describes a classical way to explain the second and third order nonlinearities in optical materials. Section 2.4 explains some symmetry properties in the third-order nonlinear susceptibility tensor. In Section 2.5, two-photon absorption in an isotropic medium as a special case of optical nonlinearity is explained and the TPA coefficient is derived from the nonlinear susceptibility tensor elements. The term *two-photon absorption* refers to the quantum mechanical explanation of this process and this is briefly

explained in Section 2.6. The last section of the chapter reviews recent research related to the applications of TPA.

2.1 Second and Third Harmonic Generation

The linear relationship between the electric field strength $E(t)$ and polarization $P(t)$ can be written as:

$$P(t) = \epsilon_0 \chi^{(1)} E(t) \tag{2.1}$$

where $\chi^{(1)}$ is the linear susceptibility. But in nonlinear optics we can write a generalized form of this equation:

$$\frac{P(t)}{\epsilon_0} = \chi^{(1)} E(t) + \chi^{(2)} E^2(t) + \chi^{(3)} E^3(t) + ... \tag{2.2}$$

Second and third term on the right hand side of Eq. 2.2 are usually of great importance in nonlinear optics and as we will see in the following subsections, these two terms explain the second and third harmonic generation in nonlinear optical materials. They are also responsible for sum-frequency generation, difference-frequency generation, four-wave mixing, self-phase modulation and self-focusing among other effects which are not discussed in this thesis.

2.1.1 Second-Harmonic Generation

As an example of the nonlinear optical process, let us consider the second term on the right hand side of Eq. 2.2 in the case that the electric field strength can be written as $E(t) = E_0 \cos(\omega t)$. The nonlinear term of the polarization will be:

$$P^{(2)}(t) = \epsilon_0 \chi^{(2)} E_0^2 \cos^2(\omega t) = \frac{\epsilon_0 \chi^{(2)}}{2} E_0^2 \left(1 + \cos(2\omega t)\right) \tag{2.3}$$

We see that the second-order polarization term consists of a zero-frequency component and a second-harmonic component. The zero-frequency term does not lead to the generation of any electromagnetic radiation, but the second term gives rise to a new electromagnetic wave with twice the input frequency [1]. In a quantum mechanical picture one can interpret this process as two input photons of frequency ω being destroyed and a single photon of frequency 2ω being simultaneously created [1].

2.1.2 Third-Harmonic Generation and Intensity-Dependent Refractive Index

If we consider the third term of the polarization and assume the same expression for the electric field strength, we can write:

$$P_{(3)} = \epsilon_0 \chi^{(3)} E_0^3 \cos^3(\omega t) = \frac{\epsilon_0 \chi^{(3)}}{4} E_0^3 \left(\cos(3\omega t) + 3\cos(\omega t)\right) \tag{2.4}$$

The first term appearing in this equation describes a response at frequency 3ω that is due to an applied field at frequency ω. This process is called third-harmonic generation and can be explained as three photons of frequency ω being destroyed and a single photon of frequency ω being created. But the second term of this equation is what we are more interested in when we talk about the two-photon absorption process. This term leads to a nonlinear contribution to the refractive index of the medium. Assuming that $\chi^{(3)}$ is a real number one can show that the refractive index of the medium will change as a function of the light intensity:

$$n = n_0 + n_2 I \tag{2.5}$$

We will consider this equation more carefully in the following sections. If $\chi^{(3)}$ has an imaginary part, this equation leads to an intensity-dependent absorption coefficient for the material.

2.1.3 General Case of the Third-Order Polarization

Now let us assume that the electric field consists of 3 different frequencies:

$$E(t) = E_1 e^{-j\omega_1 t} + E_2 e^{-j\omega_2 t} + E_3 e^{-j\omega_3 t} + \text{c.c.} \tag{2.6}$$

where c.c. means the complex conjugate of all the terms and $E(t)$ can be simplified to 3 cosine terms. If we substitute this electric field into the third-order term of Eq. 2.2 we will obtain 44 different frequency components assuming that negative and positive frequencies

Original Frequencies	$\omega_1, \omega_2, \omega_3$
Third-Harmonics	$3\omega_1, 3\omega_2, 3\omega_4$
Two-Wave Mixing	$(2\omega_1 \pm \omega_2), (2\omega_2 \pm \omega_3), ...$
Three-Wave Mixing	$(\omega_1 + \omega_2 + \omega_3), (\omega_1 + \omega_2 - \omega_3), ...$

Tab. 2.1: Different frequency components in the third-order polarization term

are distinguishable [1]. These frequency components are shown in table 2.1. This simple analysis leads us to the formal definition of the nonlinear susceptibility and writing a general form of nonlinear polarization. This general treatment is shown in Section 2.2.

2.2 Formal Definition of the Nonlinear Susceptibility

In section 2.1 we only considered the strength of the electric field and did not assume any vector nature for the field, nor did we account for the orientation of the crystal axes with respect to the propagation direction and polarization state. But none of these assumptions give us a general treatment of the nonlinear polarization and we need to consider a vector for both electric field and polarization vector. Therefore the susceptibility in general will be a tensor. First we define some parameters to be able to analyze a general case. The electric field in general has the following form:

$$\mathbf{E}(\mathbf{r}, t) = \sum_n \mathbf{E}_n e^{-j\omega_n t} + \text{c.c.} \tag{2.7}$$

Where $\mathbf{r}$ is the position vector. A spatially slowly varying field amplitude is usually defined by the following relationship:

$$\mathbf{E}_n = \mathbf{A}_n e^{j\mathbf{k}_n \cdot \mathbf{r}} \tag{2.8}$$

where $\mathbf{k}_n$ is the wave vector for frequency ω_n and $\mathbf{A}_n$ is the slowly varying amplitude for this frequency component. Considering the fact that the fields are real and defining $\mathbf{E}_n = \mathbf{E}(\omega_n)$ one can easily see that:

$$\mathbf{E}(-\omega_n) = \mathbf{E}(\omega_n)^* \tag{2.9}$$

which leads to removing the c.c. term from Eq. 2.7 and writing the general electric field as:

$$\mathbf{E}(\mathbf{r}, t) = \sum_n \mathbf{E}(\omega_n) e^{-j\omega_n t} = \sum_n \mathbf{A}(\omega_n) e^{j(\mathbf{k}_n \cdot \mathbf{r} - \omega_n t)} \tag{2.10}$$

The polarization vector resulting from this electric field will be:

$$\mathbf{P}(\mathbf{r}, t) = \sum_n \mathbf{P}(\omega_n) e^{-j\omega_n t} \tag{2.11}$$

The first, second and third order susceptibility tensors are the defined based on the following equations [8]:

$$P_i^{(1)}(\omega) = \epsilon_0 \sum_j \chi_{ij}^{(1)}(\omega) E_j(\omega) \tag{2.12}$$

$$P_i^{(2)}(\omega = \omega_1 + \omega_2) = \epsilon_0 D^{(2)} \sum_{jk} \chi_{ijk}^{(2)}(\omega_1, \omega_2) E_j(\omega_1) E_k(\omega_2) \tag{2.13}$$

$$P_i^{(3)}(\omega = \omega_1 + \omega_2 + \omega_3) = \epsilon_0 D^{(3)} \sum_{jkl} \chi_{ijkl}^{(3)}(\omega_1, \omega_2, \omega_3) E_j(\omega_1) E_k(\omega_2) E_l(\omega_3) \qquad (2.14)$$

Where $D^{(2)}$ and $D^{(3)}$ are integer factors called degeneracy factors. $D^{(2)}$ and $D^{(3)}$ represent the number of distinct permutations of the two frequencies ω_1 and ω_2 (for $\chi^{(2)}$) and the three frequencies ω_1, ω_2 and ω_3 (for $\chi^{(3)}$), respectively. $D^{(3)}$ is equal to 1 for the third-harmonic generation process (meaning that $\omega_1 = \omega_2 = \omega_3$) and is equal to 3 for intensity dependent refractive index or TPA process (meaning that $\omega_1 = \omega_2 = -\omega_3$ or two other similar combinations.) The linear susceptibility ($\chi^{(1)}$) is therefore described by a 2nd rank tensor with 3×3 elements, while $\chi^{(2)}$ is described by a 3rd rank tensor with $3 \times 3 \times 3$ elements and $\chi(3)$ is a 4th rank tensor with $3 \times 3 \times 3 \times 3$ elements. These tensors have certain properties and depending on the type of the medium one can simplify the problem by fining the zero elements of these tensors as well as the independent non-zero elements.

2.3 Classical Explanation of Nonlinear Susceptibility

The classical explanation is base on a classical anharmonic oscillator [1]. It is better to consider two cases of Noncentrosymmetric and centrocymmetric medium. For simplicity in both cases we will only consider one-dimensional motion. When no electric field is applied to the medium, the electrons are in equilibrium positions. If $x(t)$ is the amount of displacement with respect to the equilibrium position, a polarization vector of $P(t) = Nex(t)$ will be generated in the medium where N is the number of electrons per unit volume and e is the charge of an electron. Now the differential equation that explains the

motion of the electron determines how x and P are related to the applied electric field.

2.3.1 Noncentrosymmetric Medium

In this case the differential equation describing the motion of the electron is:

$$\ddot{x} + 2\gamma\dot{x} + \omega_0^2 x + ax^2 = -\frac{eE(t)}{m} \tag{2.15}$$

where γ and ω_0 are constants and a is a constant that determines the degree of nonlinearity. This differential equation considers a potential energy function of the form:

$$U = \frac{1}{2}m\omega_0^2 x^2 + \frac{1}{3}max^3 \tag{2.16}$$

that can be plotted as a function of x. The plot is shown in figure 2.1 (a) where it is easy to see that the curve is not symmetric around the equilibrium because of the second term in Eq. 2.16 that changes sign at the two sides of $x = 0$. It can be shown [1] that this term leads to a second-order susceptibility for the medium.

2.3.2 Centrosymmetric Medium

In this case the differential equation describing the motion of the electron is:

$$\ddot{x} + 2\gamma\dot{x} + \omega_0^2 x - bx^3 = -\frac{eE(t)}{m} \tag{2.17}$$

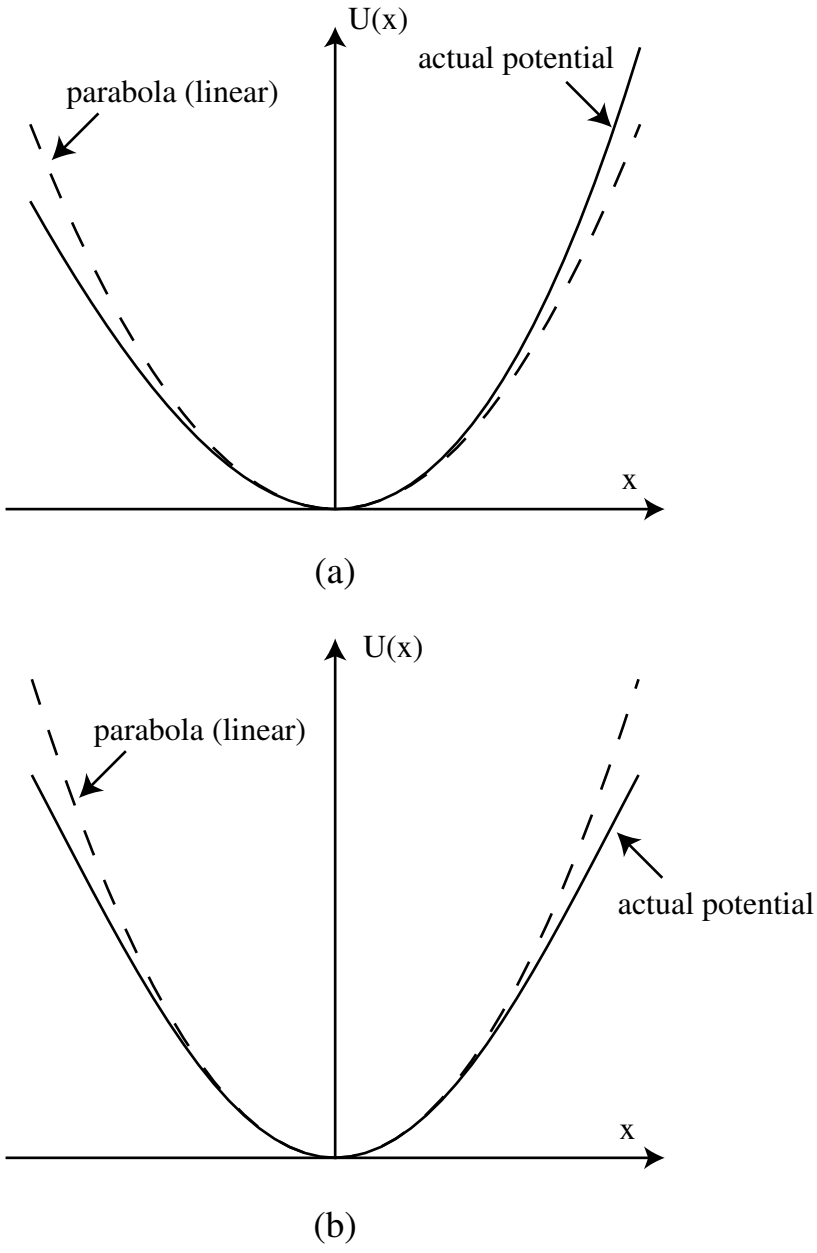

Fig. 2.1: The potential energy as a function of displacement for a noncentrosymmetric (a) and a centrosymmetric (b) medium. The dashed line shows the parabola corresponding to a linear medium. (figs/2/pot.eps)

where b is the constant that determines the degree of nonlinearity. In this case the potential energy function is:

$$U = \frac{1}{2}m\omega_0^2 x^2 - \frac{1}{3}mbx^4 \tag{2.18}$$

which gives a symmetric potential curve as shown in figure 2.1 (b). This nonlinearity leads to a third-order susceptibility in the material. We can see the difference between the two media. As we will see in the next section, the second-order susceptibility tensor elements are all zero for a centrosymmetric medium.

2.4 Symmetry Properties of the Third-Order Susceptibility

In this thesis most of the experiments and theoretical results are based on Silicon as the medium for the two-photon absorption process. Before we explain the theory of TPA process, we discuss some symmetry properties of the third-order susceptibility tensor. Silicon is a cubic crystal from the $m3m$ class and therefore it is a centrosymmetric medium. As we saw in section 2.3 all elements of $\chi^{(2)}$ tensor vanish for a centrosymmetric medium. In other words centrosymmetric system possesses inversion symmetry. Now assume that the electric field $E(t)$ generates the second-order polarization vector $P^{(2)}(t) = \epsilon_0\chi^{(2)}E(t)^2$. Because of the symmetry the inverted field $-E(t)$ should generate a polarization equal to $-P^{(2)}(t)$ but this means that $\chi^{(2)}$ has to be zero. So the third-order susceptibility gives the first non-zero nonlinear term. Table 2.2 gives a brief overview on the susceptibility tensor in some media. As we can see in the table in an isotropic medium there are only 3 indepen-

Medium	Number of non-zero and independent elements
Isotropic	21, 3
Cubic crystal classes $m3m$,432,$\overline{4}3m$	21, 4
Cubic crystal classes $m3$,23	21, 7
Orthorhombic crystal	21, 21
Triclinic crystal	81, 81

Tab. 2.2: Form of the $\chi^{(3)}$ tensor for a few media [1]

Medium	Non-zero elements
Isotropic	$yyzz = zzyy = zzxx = xxzz = xxyy = yyxx$ $yzyz = zyzy = zxzx = xzxz = xyxy = yxyx$ $yzzy = zyyz = zxxz = xzzx = xyyx = yxxy$ $xxxx = yyyy = zzzz = xxyy + xyxy + xyyx$
$m3m$ crystal	$yyzz = zzyy = zzxx = xxzz = xxyy = yyxx$ $yzyz = zyzy = zxzx = xzxz = xyxy = yxyx$ $yzzy = zyyz = zxxz = xzzx = xyyx = yxxy$ $xxxx = yyyy = zzzz$

Tab. 2.3: Non-zero elements of $\chi^{(3)}$ tensor for isotropic and $3m3$ cubic crystal. [1]

dent values that must be determined to completely specify the susceptibility tensor of the medium. In silicon which is a $m3m$ crystal the number of independent values is 4. Now let us consider the third-order susceptibility tensor of the isotropic material and cubic $m3m$ crystal and give a more detailed image of this tensor. Table 2.3 shows the non-zero elements of $\chi^{(3)}$ tensor. In this table the indices are shown and $\chi^{(3)}$ is eliminated, for example $xxyy$ means $\chi^{(3)}_{xxyy}$. In the next section we will explain the two-photon absorption process and derive an expression for TPA coefficient in an isotropic medium. The other symmetry

properties of the third-order susceptibility tensor are that:

- For a third-harmonic generation (THG) process when $\omega_1 = \omega_2 = \omega_3$ the intrinsic permutation symmetry of $\chi^{(3)}$ requires that:

$$\chi^{(3)}_{iijj} = \chi^{(3)}_{ijij} = \chi^{(3)}_{ijji} \tag{2.19}$$

- For a TPA process or intensity-dependent refractive index when $\omega_1 = \omega_2 = -\omega_3$ or two other similar combinations, the intrinsic permutation symmetry requires that:

$$\chi^{(3)}_{ijij} = \chi^{(3)}_{iijj} \tag{2.20}$$

2.5 Two-Photon Absorption Coefficient for an Isotropic Medium

In section 2.1.2 we discussed the intensity-dependent refractive index as a result of the third-order nonlinearity in the medium. Eq. 2.5 gives a formula for the refractive index that is proportional to the intensity of the light. Now if n_2 in Eq. 2.5 is a complex number and has a non-zero imaginary part, then this leads to an intensity-dependent absorption coefficient. This is what we call two-photon absorption. In this section we will consider this phenomenon more carefully and in more detail based on Eq. 2.14.

In Eq. 2.14 if $(\omega_1, \omega_2, \omega_3) = (\omega, \omega, -\omega)$, then the output polarization has a frequency

of ω. But considering Eq. 2.9 we can rewrite Eq. 2.14 for the case of TPA process as:

$$P_i^{(3)}(\omega) = 3\epsilon_0 \sum_{jkl} \chi_{ijkl}^{(3)} E_j(\omega) E_k(\omega) E_l^*(\omega) \tag{2.21}$$

Now to find the absorption coefficient we should write the wave propagation equation in this medium. Combining two of Maxwell's equations in a source-free and non-magnetic medium:

$$\nabla \times \mathbf{E} = -\mu_0 \frac{\partial \mathbf{H}}{\partial t} \ , \ \nabla \times \mathbf{H} = \frac{\partial \mathbf{D}}{\partial t} \tag{2.22}$$

we obtain the general form of the wave equation:

$$\nabla \times \nabla \times \mathbf{E} + \mu_0 \frac{\partial^2 \mathbf{D}}{\partial t^2} = 0 \tag{2.23}$$

Writing $\mathbf{D}$ in terms of $\mathbf{E}$ and $\mathbf{P}$ and separating $\mathbf{p}$ into a sum of linear and nonlinear terms, we have:

$$\mathbf{D} = \epsilon_0 \mathbf{E} + \mathbf{P} = \epsilon_0 n^2 \mathbf{E} + \mathbf{P}^{NL} \tag{2.24}$$

Where $\mathbf{P}^{NL}$ is the nonlinear term in the polarization vector which in the current case is the third-order nonlinearity. n is the linear (intensity independent) refractive index of the medium. The $\nabla \times \nabla$ operator can be reduced to $-\nabla^2$ provided the refractive index of the medium is spatially invariant which is true for a linear homogeneous medium, and approximately true for the nonlinear materials considered in this work. Now combining

these equations we get to the nonlinear wave equation:

$$-\nabla^2\mathbf{E}(\mathbf{r},t)+\frac{n^2}{c^2}\frac{\partial^2 E(\mathbf{r},t)}{\partial t^2}=-\mu_0\frac{\partial^2\mathbf{P}^{NL}(\mathbf{r},t)}{\partial t^2} \tag{2.25}$$

In the sinusoidal regime assuming fields with frequency ω we can rewrite this equation in this form:

$$-\nabla^2\mathbf{E}(\mathbf{r},\omega)-\frac{n^2\omega^2}{c^2}\mathbf{E}(\mathbf{r},\omega)=\mu_0\omega^2\mathbf{P}^{NL}(\mathbf{r},\omega) \tag{2.26}$$

Now assume that we have a linearly polarized light propagating as a plane wave and since the medium is isotropic we can take the (x,y,z) coordinate system such that the electric field is linearly polarized along the x axis and the z axis is the direction of propagation of the wave. Substituting the single component electric field in Eq. 2.21 we get:

$$P_x^{(3)}(\omega)=3\epsilon_0\chi^{(3)}_{xxxx}E_x(\omega) \tag{2.27}$$

substituting this in Eq. 2.26 gives:

$$\frac{\partial^2 E_x(z)}{\partial z^2}+\frac{n^2\omega^2}{c^2}E_x(z)=-3\frac{\omega^2}{c^2}\chi^{(3)}_{xxxx}\left|E_x(z)\right|^2E_x(z) \tag{2.28}$$

The nonlinear term can be thought of as a small perturbation in the linear wave equation. If $A(z)$ is the slowly-varying amplitude of the wave and $k=\dfrac{n\omega}{c}$ is the propagation constant

of the wave in the low-intensity limit, we have:

$$E_x(z,\omega) = A(z)e^{-jkz} \tag{2.29}$$

And by substituting this in Eq. 2.28 we can find the differential equation showing the variation of $A(z)$ as a function of z. Since $A(z)$ slowly varies with z we can neglect the term including $\frac{d^2A}{dz^2}$ and by simplifying the equation we obtain this equation:

$$\frac{dA(z)}{dz} = j\frac{3\omega}{2nc}\chi^{(3)}_{xxxx}\left|A(z)\right|^2 A(z) \tag{2.30}$$

In this equation $\chi^{(3)}_{xxxx} = \mathsf{Re}(\chi^{(3)}_{xxxx}) + j\mathsf{Im}(\chi^{(3)}_{xxxx})$ and there will a real and an imaginary term for $\frac{dA}{dz}$. But the real term is the one that gives the TPA coefficient and in order to find this coefficient we only consider the real part of $\frac{dA}{dz}$ which comes from the imaginary part of $\chi^{(3)}_{xxxx}$. Therefore we have:

$$\frac{dA(z)}{dz} = -\frac{3\omega}{2nc}\mathsf{Im}(\chi^{(3)}_{xxxx})\left|A(z)\right|^2 A(z) \tag{2.31}$$

Now let us go back to Eq. 2.7 where we assumed the electric field corresponding to a wave of frequency ω can be written as $E_x e^{-j\omega t} + E_x^* e^{+j\omega t}$. This form of treating the problem keeps the electric field a real number although we use complex analysis to solve the

problem. The time-average intensity of light is [1]:

$$I = 2n\left(\frac{\epsilon_0}{\mu_0}\right)^{1/2}|E_x|^2 = 2n\left(\frac{\epsilon_0}{\mu_0}\right)^{1/2}|A|^2 \tag{2.32}$$

And by this formula we can write $\frac{dI}{dz}$ in terms of the evolution of $A(z)$:

$$\frac{dI(z)}{dz} = 2n\left(\frac{\epsilon_0}{\mu_0}\right)^{1/2}\left(A(z)\frac{dA^*(z)}{dz} + A^*(z)\frac{dA(z)}{dz}\right) \tag{2.33}$$

And by combining this equation and Eq. 2.31 we have:

$$\frac{dI(z)}{dz} = -\frac{3\omega}{2\epsilon_0 n^2 c^2}\mathsf{Im}(\chi^{(3)}_{xxxx})I^2(z) \tag{2.34}$$

The TPA coefficient β will be:

$$\beta = \frac{1}{I^2}\frac{dI}{dz} = \frac{3\omega}{2\epsilon_0 n^2 c^2}\mathsf{Im}(\chi^{(3)}_{xxxx}) \tag{2.35}$$

Eq. 2.34 shows that the amount of absorbed power in a thin layer of the medium is proportional to the square of the light intensity (or power). This result is important because we can use this process to make a nonlinear detector. The two-photon absorbed power is usually much smaller that the incident power, in this case the detector based on TPA process will

have a photocurrent proportional to the power squared [1]:

$$i_{TPA} = KP^2 \tag{2.36}$$

where K is a proportionality constant that depends on β, the focused spot size, and the geometry of the medium.

As we mentioned before this treatment applies for an isotropic medium. Also the light polarization is considered to be linear. In Chapter 4 we will discuss in more detail how anisotropy or elliptical polarization of the light would change the TPA response.

2.6 Quantum Mechanical Interpretation of Two-photon Absorption

In this section we give a brief and simple explanation based on quantum mechanics about two-photon absorption which will actually show why the process is called two-photon absorption. Assume that we have a semiconductor material with an energy bandgap E_g. A single photon with energy $h\nu \geq E_g$ is able to generate a single electron-hole pair and therefore we see a linear absorption in such a material. But now suppose that the energy of the photon is lower such that $h\nu \leq E_g \leq 2h\nu$. In this situation one photon is not able to move an electron from the lower edge to the upper edge of the bandgap. But a single electron-hole pair may be produced by the instantaneous absorption of two photons. Figure

[1] For example if the detector is a slab of thickness Δz and $\beta I \Delta z \ll 1$ we can write $\Delta I \simeq \beta I^2 \Delta z$ where ΔI is the change in the intensity of the light passing through the slab. This is equivalent to Eq. 2.36

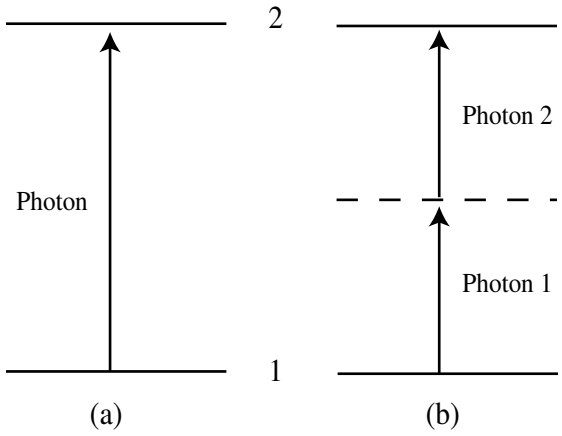

Fig. 2.2: The absorption of photons in a two-level system, (a) linear (single-photon) absorption and (b) two-photon absorption. (figs/2/pot.eps)

2.2 shows a simple diagram of what happens in a linear absorption (a) and two-photon absorption (b). As seen in the figure the absorption occurs by taking the electron to a virtual state by the energy from the first photon and almost simultaneously moving it to the final state by means of the second photon. This process has been discussed mathematically in most of nonlinear optics or quantum mechanics book [1, 9]. One can show that increasing the intensity of the light (or the number of photons per second incident on the material) will increase the probability of the process and therefore the absorption is nonlinear. In [9] it is shown that the absorption coefficient of the medium is proportional to the intensity of the light which means that the photocurrent is proportional to the square of the incident optical power.

2.7 Applications of two-photon absorption

Two-photon absorption as a nonlinear process is an attractive candidate for a number of applications. This process because of its nonlinear nature is sensitive to compression of optical power both is time and space domains. Especially the sensitivity of TPA process to the compression of optical power in time has widely been used to build systems for auto-correlation, cross-correlation, measurement of very short pulses and also optical communication applications. The other important feature of TPA process that makes it more attractive for these types of applications is that the response time of the process is very short and therefore can be used for high speed communication systems or ultrashort pulses. In this chapter we will introduce some of these applications based on the literature.

2.7.1 Autocorrelation and Crosscorrelation

Autocorrelation techniques are mostly important because they give a method for pulse-width measurement for ultrashort optical pulses. Different methods have been used including different nonlinear processes but a very common method that has recently been used is the two-photon absorption. The beam of light from the optical pulse source is split into two beams and one of the beams undergoes a controlled time delay, then both beams are incident on a photodetector with TPA response. The output current of the detector will have a constant background when the two pulses from the two beams do not overlap and it will increase if the two pulses have some overlap with each other. This is the main concept

of building autocorrelator based on TPA process. This happens because the output of the TPA detector is proportional to the square of the optical power or the fourth power of the electric field amplitude. In [10] an autocorrelation measurement based on TPA in a GaAsP photodiode is reported that is able to measure pulses as short as 6 fs. A highly sensitive autocorrelator using Si avalanche photodiode as a two-photon absorber is also introduced in [11]. The same method can be modified to be used as a crosscorrelation measurement technique by using two different signals. In [12] a crosscorrelator based on TPA in a Si avalanche photodiode is used for measurement of picosecond pulse transmission characteristics.

2.7.2 All-Optical Demultiplexing and Sampling

Future development of high capacity optical time division multiplexed (OTDM) systems can only happen by using ultra-fast switching techniques. But it has been well understood that constructing high speed optical switches requires employing all-optical techniques which usually means using nonlinear effects. Different techniques based on different nonlinear effects have been reported. One of these techniques is based on TPA process and works with the same principle as what was explained in Section 2.7.1. The system utilizes an optical control pulse to demultiplex a high speed OTDM channel via the TPA nonlinearity. This method has been reported in [13] using TPA in a laser diode. The principle of operation is very easy to understand. If the power of the signal is P_s and the the control signal has a power of $P_c \gg P_s$, then the average TPA output current when the two pulses

do not have any overlap will be:

$$i = K(P_s^2 + P_c^2) \simeq KP_c^2 \tag{2.37}$$

and when they have a full overlap we have:

$$i = K(P_s^2 + 2P_sP_c + P_c^2) \simeq K(P_c^2 + 2P_cP_s) \tag{2.38}$$

This equation shows that the average photocurrent has a constant background that increases when the control and signal pulses overlap.

A similar method is used to make an all-optical sampling system that can be used as optical oscilloscope. In this system that is reported in [14] a relatively high power sampling pulse is injected at the same time with a signal pulse on TPA detector which is a waveguide. A similar analysis to Eq. 2.38 shows a cross-term which is a function of the time delay between the signal and the sampling pulses and for short sampling durations one can show that the cross-term gives the shape of the signal pulse.

2.7.3 Optical Thresholding

The TPA process can distinguish between two optical pulses with the same energy and different time durations. For simplicity consider two periodic pulse trains with period T. One of the pulses has peak power $2P$ and duration $\frac{\tau}{2}$ and the other has peak power P and

duration τ. Both pulses have average power of $P_{\text{ave}} = \frac{P\tau}{T}$, therefore a slow linear detector can not show any difference between the two pulses. But the average TPA photocurrent generated by the two pulses will be:

$$\begin{aligned} i_1 &= 2K\frac{P^2\tau}{T} \\ i_2 &= K\frac{P^2\tau}{T} \end{aligned} \tag{2.39}$$

An optical Thresholder is a system that can distinguish between properly and improperly decoded signals using the contrast in their peak intensity. A correctly coded waveform gives a short and intense pulse after being decoded whereas an incorrectly coded signal will give a pulse with lower peak power and longer duration. Such a system in introduced in [15] as a suitable all-optical signal processing tool for the coherent ultrashort pulse CDMA systems.

2.7.4 Chirp Measurement

The chirp measurement is very similar to optical thresholding system. In a chirp measurement the most important parameter of the pulse that can be measured is the width of the pulse. As an unchirped pulse goes through a dispersive medium it spreads in time and therefore TPA process is suitable for detecting this change in the pulse duration. In [16] this method and the system built to measure the chirp are explained.

2.7.5 Other Applications

In this section we summarize some other applications of TPA that have been reported in the literature. Reduction of optical intensity noise is done by using the TPA in ZnSe [17]. In this work it is shown that the fluctuations in the intensity of a laser can be reduced by means of a two-photon absorber. Infrared image detection with a Si-CCD image sensor that uses the TPA in this detector is reported in [18]. The method is based on the autocorrelation of the light intensity in this sensor by means of TPA process. Two-photon absorption spectroscopy is the other application for TPA that has been discussed in [8] and an experimental work is reported in [19]. Finally a reflectometry method based on TPA in a Si avalanche photodiode is reported in [20].

3. SENSITIVITY ISSUES IN TWO-PHOTON ABSORPTION

In the previous chapter we discussed two-photon absorption as a nonlinear susceptibility in the optical material besides looking briefly at the quantum mechanical explanation of the phenomenon. In the current chapter we focus on the generation of two-photon absorption current in a photo detector. In optical communication systems we are interested in the wavelength of 1550 nm and a good candidate for the detection of TPA signal is silicon. Silicon has an energy band-gap more than the photon energy at 1550 nm and therefore does not have any linear absorption in this wavelength. But since the band-gap of silicon is less that twice the photon energy, some two-photon absorption can be observed. This is explained more in Section 3.1. Observing two-photon absorption in a detector is the first issue discussed in this chapter and all of the experimental results given in the chapter are generated with the experimental setup introduced in Section 3.1. There are a number of factors that determine the TPA photo-current of a detector and the main goal of the chapter is to define and quantify these factors. Section 3.2 shows the experimental results taken from the setup introduced in Section 3.1. Section 3.2.3 gives an experimental result showing the effect of the long-pass filter on the current-power curve of the detector. In Section 3.3 we will see how the two-photon absorption depends on the spot size of the beam

focused on the photo-detector. In Section 3.4 we show the experiment used to determine the spot size for different lenses. Section 3.5 presents a theoretical model of the detector that gives a more realistic formula for the effect of spot-size on the TPA current. The experimental data confirming the theoretical results in Section 3.5 is given in section 3.6. As mentioned before there are a variety of factors affecting the sensitivity of TPA process in a detector. One other effect is the anti-reflection coating designed for low wavelengths on commercial photo-detectors. This parameter is discussed in Section 3.7 of this chapter. The last section of this chapter examines how the two-photon absorption varies over the detector surface, in comparison with the single-photon absorption process.

3.1 Experimental setup to study two-photon absorption

Before giving a schematic of the experimental setup used for the research we summarize the main requirement for a system to be able to show two-photon absorption.

1. *Suitable Detector*: The detector used should be made of a material with a band-gap in the range $(h\nu, 2h\nu)$ where ν is the frequency of the light. For wavelength of 1550nm a Si avalanche photodiode (APD) is a good choice since Silicon has this property ($E_g \simeq 1.12$ eV which is about $1.4h\nu$ at 1550 nm) and also the internal gain provided by an APD makes it easier to see the small signal due to the TPA.

2. *Focusing the light*: Two-photon absorption as explained later in Section 3.3 is very sensitive to the spot size of the light incident on the detector. The smallest spot can

usually be the best choice and that is why using a focusing lens right before the detector is necessary.

3. *Long-Pass filter*: In some cases the light incident on the detector may have frequency components in the normal absorption range of the detector. For when an EDFA is used, a weak 980 nm residual pump component may be in the output of the amplifier which can give a linear absorption photocurrent comparable to the two-photon absorption. In order to avoid this we used a long-pass filter at 1200nm in our experiment.

4. *Fine movement of the detector*: It is very important to align the system to get a beam normal to the surface of the detector and also adjust the detector to be on the focal plane of the focusing device. This can only be done by means of a precise translation stage.

5. *Output noise reduction*: The output of the detector can be so small that using a lock-in detection system may be necessary, especially in the initial alignment process. In our system a chopper and lock-in amplifier is used.

6. *Polarization control*: As we will see later in Chapter 4 two-photon absorption is also sensitive to the polarization state of light. In the experiment we need to tape all the movable optical components and fibers to the table in order to avoid the change in polarization affect the experiment. We also used a polarization controller, a linear polarized and waveplates to study the polarization dependence of the TPA process.

Considering these requirements we set up an experiment which is the main setup used for most of the experiments in the following sections. The schematic of the experiment is shown in figure 3.1.

In this setup the power of the laser is increased to about 100 mW using an EDFA and 5 percent of this power is tapped off with a coupler to be used to monitor the input power to the system. An inline polarization controller is used to study the polarization sensitivity of the TPA process. A variable attenuator changes the input power to the collimator. After point A in the figure the system in under a box to minimize the effect of room light. Light coming out of the collimator is chopped using a chopping wheel. A linear polarizer and quarter- or half- waveplate are used in the experiments of polarization sensitivity. LPF as mentioned before is a long-pass optical filter at 1200 nm that eliminates the optical radiation with short wavelengths. The focusing lens is usually a microscope objective that focuses the collimated light into a very small spot (a few microns) on the surface of the detectors. The detector used in the TPA experiment is a Si avalanch photodiode (APD) and is followed by an amplifier to convert the photocurrent to voltage. A translation stage is used to align the detector to the incident beam and adjust the location of the detector on the focal plane of the lens. More details about the devices and instruments used in this setup are given in Appendix A.

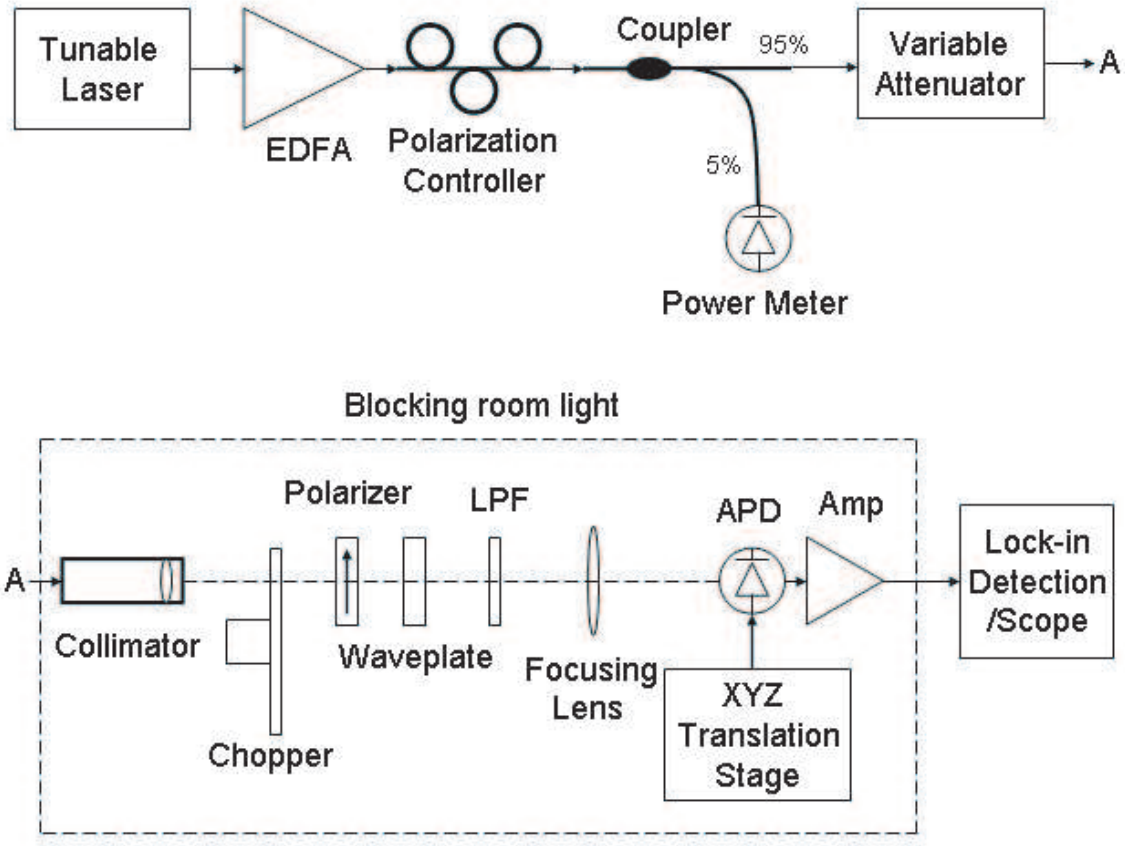

Fig. 3.1: Experimental setup used for observing TPA process (figs/3/setup.eps)

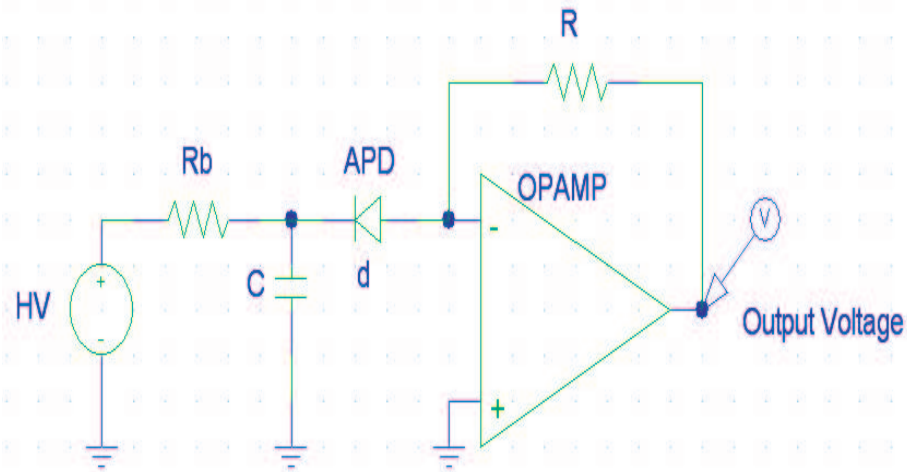

Fig. 3.2: Schematic of the circuit used to convert the photocurrent to voltage (figs/3/circuit.eps)

3.1.1 Detector circuit

The APD detector needs a high voltage source (about 200 V) to provide the required voltage for the avalanche process. The photocurrent generated in the detector is converted to voltage using the circuit shown in figure 3.2. In this circuit HV shows the high voltage supply and Rb is the bias resistor. Appendix A shows more details about the circuit.

3.1.2 Alignment Technique

The TPA photocurrent is very sensitive to the alignment of the system. The reason is that the laser can only provide enough intensity for a measurable TPA process when it is focused

to a very small spot on the detector. In order to align the system we initially use a 980 nm laser (which produces a single-photon absorption) and maximize the photocurrent. This allows for coarse alignment of the detector, because the linear photocurrent is much less sensitive to the detector position. After the coarse alignment, the system is connected to a 1550 nm source when we should be able to observe TPA current. This is possible by moving the detector in the z direction and finding the focal point of the focusing lens.

3.2 Two-photon Absorption Experimental Results

The system described in the previous section gives a good observation of the TPA process in silicon. In this part of the experiment a 10× microscope objective is used as the focusing lens and the power of the beam is changed using the attenuator. The output voltage measured by the lock-in detector is plotted vs. the input power to the detector in figure 3.3. The measurement of the power is explained in Section 3.2.1. As seen in the figure the slope of the curve is very close to 2 decades of photocurrent per decade of optical power in a log-log scale and it shows a saturation effect as the power is increased. Figure 3.3 shows the points taken from the experiment and also the ideal two-photon absorption curve corresponding to the equation:

$$V_{LIA} = RP^2 \tag{3.1}$$

In this equation V_{LIA} is the voltage read from the lock-in amplifier and P is the power focused on the detector. R is the equivalent of responsivity for the TPA case. From this

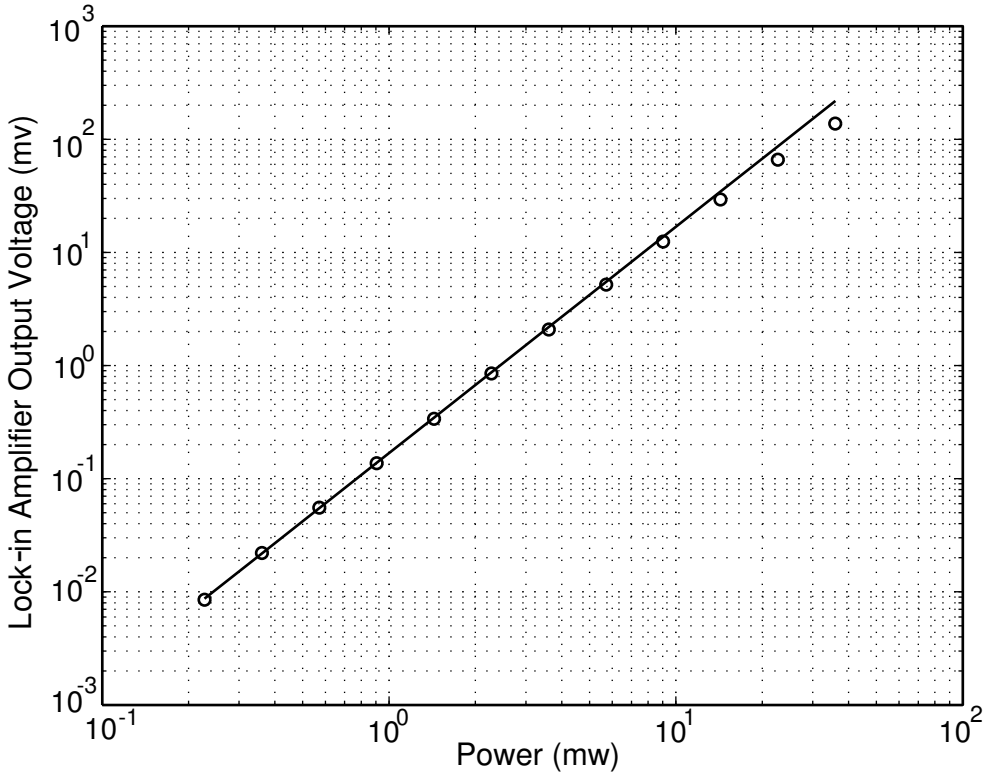

Fig. 3.3: Output voltage vs. input power showing a slope of 2 in the log-log scale.
(figs/3/tpa.eps)

experimental data as seen in the figure, the input power range to see two-photon absorption effect without any saturation is:

$$0.2\,\mathrm{mW} < P < 10\,\mathrm{mW} \tag{3.2}$$

Off course the lower limit is due to the noise limitation but the upper limit is because of the saturation effect. This power range gives an output voltage range of:

$$0.01\,\mathrm{mV} < V_{LIA} < 10\,\mathrm{mV} \tag{3.3}$$

The value of R calculated from this range is:

$$R \simeq 0.168 \frac{\mathrm{mV}}{\mathrm{mW}^2} \tag{3.4}$$

3.2.1 Calibration of the input power

The incident power to the detector was measured using a power meter installed at the focal plane of the lens. The power plotted on the horizontal axis of figure 3.3 refers to the constant power not the chopped power. In other words the power is measure when optical signal is unchopped. The attenuation is then multiplied by this measured power. The power monitor at the 5% output of the detector is to account for any power fluctuations that may occur.

3.2.2 Photocurrent calculation

The photocurrent when power is ON can be related to the the voltage being read on the display of the lock-in amplifier. If V is the output of the circuit shown in figure 3.2 and i is the photocurrent we have: $i = \frac{V}{R}$ where R is the resistor shown in figure 3.2. But the output of the lock-in amplifier can be related to the ON voltage of the circuit using the relationship: $V \cong 2.7V_{LIA}$ where V_{LIA} is the lock-in amplifier voltage. Therefore finally assuming $R = 200$ kΩ we have:

$$i(\mu\mathrm{A}) \simeq 0.0135V_{LIA}(\mathrm{mV}) \tag{3.5}$$

3.2.3 Effect of the Long-pass Filter

The fiber amplifier used in these experiments contains a pump laser operating at 980 nm. The isolator and WDM coupler at the output of this device should ideally remove all 980nm radiation but there may be a weak residual 980 nm light coming out of the EDFA. In this part of the experiment we removed the long-pass filter to see the difference between the filtered and not filtered inputs. The output is plotted in figure 3.4 and the dashed line shows the line with slope of 2 corresponding to the TPA process. The slope of the curve at low powers is closer to 1 as expected for single-photon absorption. Single-photon absorption is easier to see at lower powers because TPA photocurrent is proportional to the square of the power and decreases more rapidly when power is decreased. In figure 3.4 two dashed lines

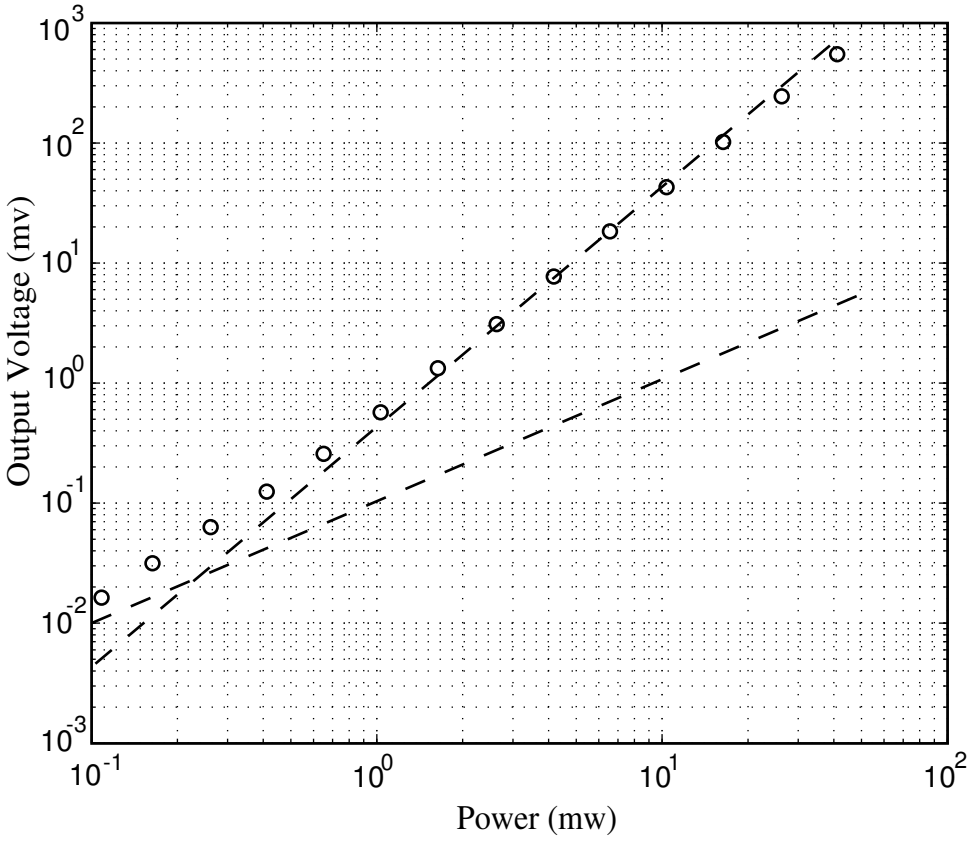

Fig. 3.4: Output voltage of the detector when LP filter is removed. Dashed lines show the lines with slope of 1 and 2 corresponding to the linear absorption and the TPA process (figs/3/filter.eps)

show the two lines corresponding to single-photon and two-photon absorption processes. This experiment proves that using the LP filter is of great importance in TPA experiments and there is always some residual low frequency power in the beam coming out of the EDFA. This would not be an issue for GaAs devices and it could also be avoided if we used a 1480 nm pumped EDFA.

3.3 Spot-size Sensitivity

Assume a single-photon absorption process in a detector from a beam focused to a very small spot so that the spot is completely inside the detector area. In this case as long as the detector includes the whole spot, the photocurrent generated by the detector should remain almost the same. Mathematically if the photocurrent generated from the area dA of the detector is di then one can write: $di = k_1 I dA$ where I is the intensity of the light at that point and k_1 is a coefficient that relates the current to the power. Using this formula for a Gaussian beam [1] from a lens with the spot size of w_0 centered on a detector with a radius of R we can write:

$$i = \int di = k_1 I_0 \int_0^R \exp\left(-\frac{2r^2}{{w_0}^2}\right) 2\pi r dr = \frac{1}{2} k_1 I_0 \pi w_0^2 \left[1 - \exp\left(-\frac{2R^2}{{w_0}^2}\right)\right] \tag{3.6}$$

$$i = k_1 \left[1 - \exp\left(-\frac{2R^2}{{w_0}^2}\right)\right] P \tag{3.7}$$

[1] See Appendix B for the Gaussian beam formulation

Where I_0 is the peak intensity of the beam, P is the total power of the beam and r is the cylindrical coordinates radius. This calculation shows that for $R \gg w_0$ the current is almost constant and is equal to $k_1 P$ where P is the total optical power of the beam. In our experiment the radius of the detector is about $250\mu m$ and w_0 from the focusing lens is a few microns only. Therefore no significant change in the linear photocurrent is expected if the spot size changes.

Now let us look at the similar case with the two-photon absorption phenomenon. The model for this two dimensional detector can be written as: $di = k_2 I^2 dA$ where k_2 is a constant. In this case, if all other parameters of the beam and detector are the same as single-photon absorption case we can write:

$$i = \int di = k_2 I_0^2 \int_0^R \exp\left(-\frac{4r^2}{{w_0}^2}\right) 2\pi r dr = \frac{1}{4} k_2 I_0^2 \pi w_0^2 \left[1 - \exp\left(-\frac{4R^2}{{w_0}^2}\right)\right] \tag{3.8}$$

$$i = \frac{k_2}{\pi w_0^2} \left[1 - \exp\left(-\frac{4R^2}{{w_0}^2}\right)\right] P^2 \tag{3.9}$$

In this analysis one can easily see that the photocurrent strongly depends on the spot size of the beam (w_0). According to this simple model, the photocurrent increases as $\frac{1}{w_0^2}$ by making the spot size smaller. But as we will see in section 3.5 this is not true and depending on the thickness of the absorbing medium this regime changes.

Since the spot-size plays a significant role in the TPA process we measured the beam spot-size produced by two different focusing lenses and the results are given in the next

section.

3.4 Spot-size Measurement

The focusing lenses used in this experiment are two microscope objectives with $10\times$ and $20\times$ magnifications. The optical features of these lenses are given in table 3.1. In this table EFL and NA stand for effective focal length and numerical aperture of the lens. The collimated beam has a beam width of about 5.5 mm that covers the whole area of both lenses. Also the calculation of spot-size is based on the following approximate formula:

$$w_0 \simeq \frac{\lambda}{2\mathrm{NA}} \tag{3.10}$$

The experimental setup to measure w_0 is based on measuring a Gaussian beam intensity distribution in the far-field. Measurement of w_0 at the focal point can be hard and inaccurate due to the small dimensions of the spot-size but we can measure the diffracted beam far from the focal point and infer the focal point spot-size using the Gaussian beam for-

Magnification	**NA**	**EFL (mm)**	**Working Distance (mm)**	**Calculated $\mathbf{w_0}$ (μm)**
$10\times$	0.25	17.13	6.14	3.1
$20\times$	0.4	8.55	3.3	1.94

Tab. 3.1: Optical features of two microscope objective lenses including calculated spot-size based on the numerical aperture of the lens

mulation. The experimental setup in shown in figure 3.5. The collimated beam is focused to a small spot and the beam profile is measured at a distance z from the focal point. The measurement of the beam profile is accomplished with a 1550nm detector that is moved along the radial direction by means of a one-directional translation stage. The translation stage measures the position of the detector with a precision of 1 mil or 25 μm . In figure 3.5, r is the radial distance from the axis of the beam and the area of the detector is assumed to be much smaller than the size of the diffracted beam which means than the intensity at each point is proportional to the power detected by the linear photodetector.

From Gaussian beam formulation we have:

$$I(r) = I(r=0)\exp\left(-\frac{2r^2}{w(z)^2}\right) \Rightarrow V(r) \simeq V(r=0)\exp\left(-\frac{2r^2}{w(z)^2}\right) \tag{3.11}$$

In this equation I and V are the intensity and detector output voltage respectively and $w(z)$ is the spot size at a point z (mm) far from the focal point. Data points of (r, V) are plotted in MATLAB and $w(z)$ is determined by performing a least-square fit to Eq. 3.11. The two plots corresponding to both lenses are given in figure 3.6 and the numerical value for $w(z)$ from the fitting program is indicated on the figures.

Now it is easy to find w_0 from $w(z)$ by using the following formula:

$$w(z)^2 = w_0^2\left[1 + \left(\frac{z}{z_0}\right)^2\right] \tag{3.12}$$

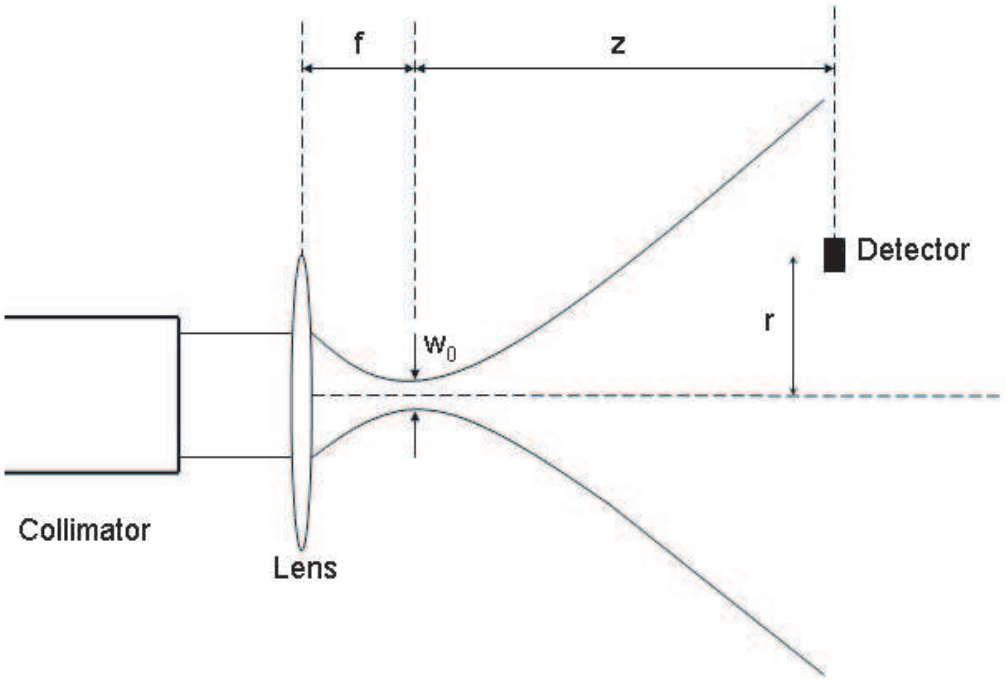

Fig. 3.5: Beam radius measurement experiment (figs/3/beamsize.eps)

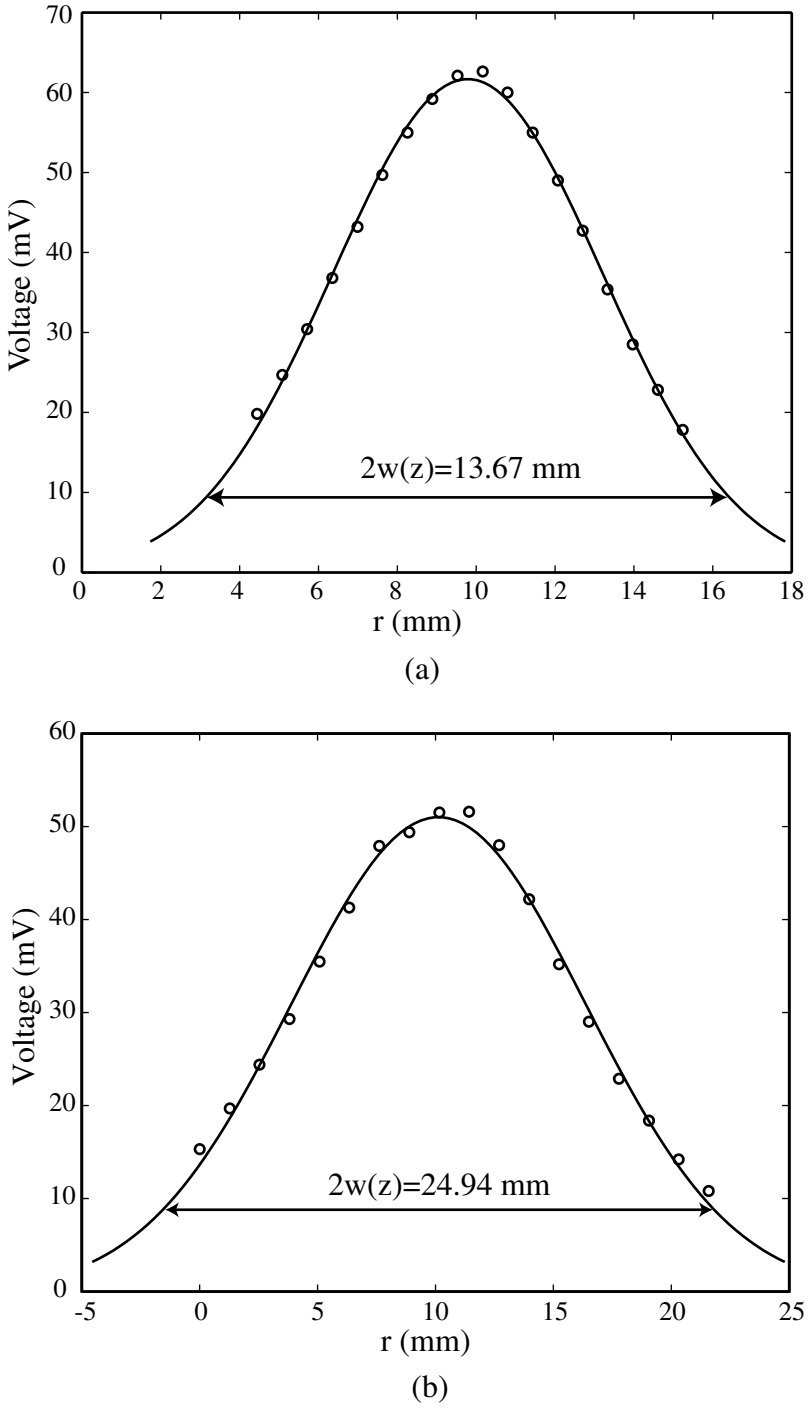

Fig. 3.6: Measured gaussian profile of the beam for two lenses: microscope objective with 10× magnification (a) and microscope objective with 20× magnification (b) (figs/3/beam.eps)

Magnification	z (mm)	w(z) (mm)	Measured $\mathbf{w_0}$ (μm)	Calculated $\mathbf{w_0}$ (μm)
10×	45.4	6.84	3.28	3.1
20×	44.7	12.47	1.77	1.94

Tab. 3.2: Measured values for the spot-size measurement experiment and comparison with the calculated values

where $z_0 = \frac{\pi w_0^2}{\lambda}$ is the confocal beam parameter. Table 3.2 gives the calculated and measured beam sizes for the two lenses. This measurement shows a good agreement with the calculation based on the numerical aperture and therefore is an accurate method for spot-size measurement. In the next section we discuss a more detailed model for the spot-size effect on TPA photocurrent in a detector.

3.5 Further Considerations in the Spot-size Sensitivity

In section 3.3 we considered a very simple two-dimensional model for the TPA photocurrent generation in a circular detector. In practice the thickness of the absorption region is not negligible compared to the confocal beam parameter (z_0) and therefore should be considered in the calculations. Two examples of the typical structure of Si avalanche photodiode is shown in figures 3.7 (a) and (b) [3]. In both structures the absorption of light occurs in the intrinsic region labeled as π and the avalanche process occurs in the p region which can be in the front or back of the intrinsic region and is connected to a n^+ region. The thickness of the intrinsic (lightly doped) absorbing region is typically 50-100 μm,

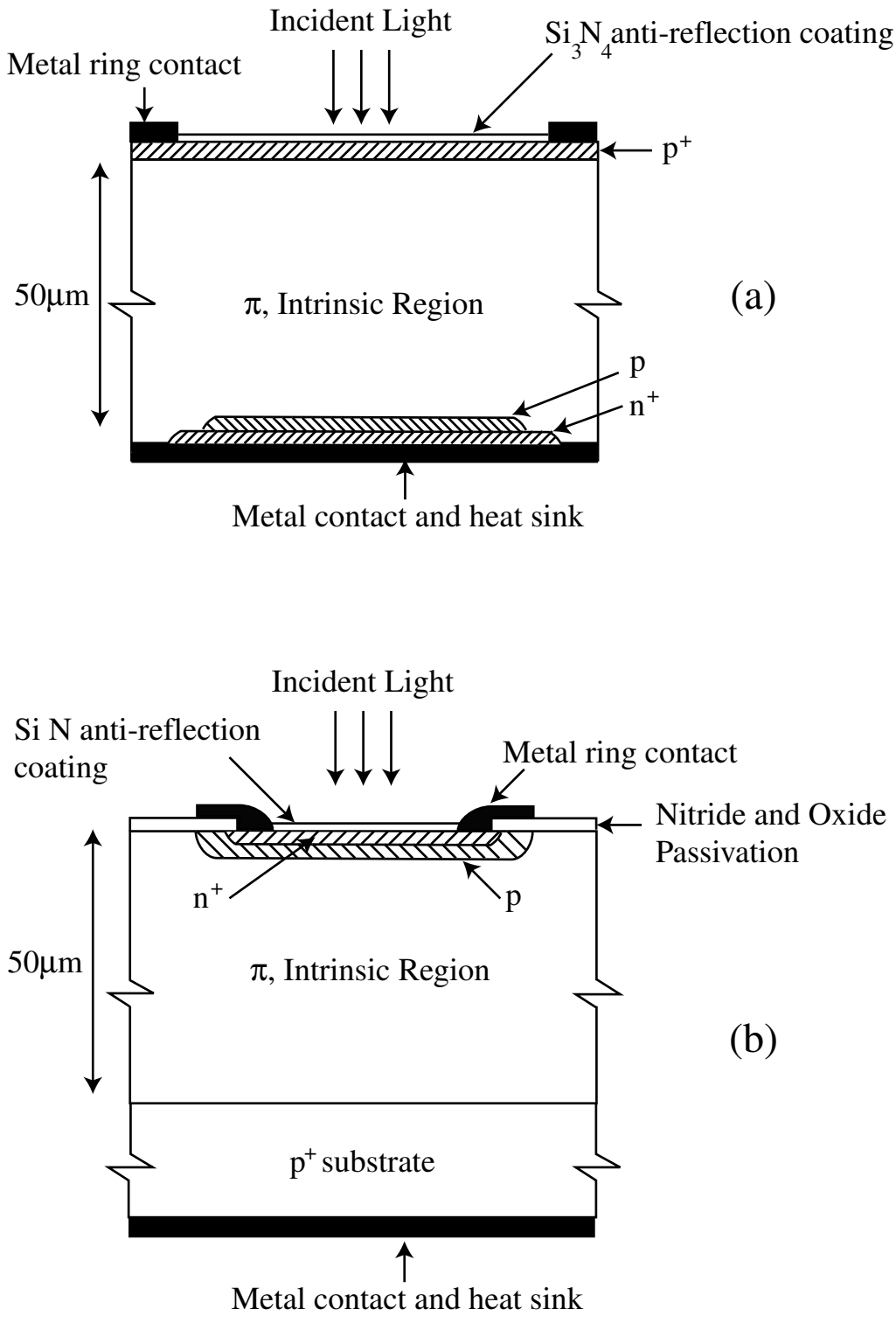

Fig. 3.7: Structure of Si Avalanche Photodiode. The avalanche region can be in the back (a) or in front (b) of the absorption region [3]. (figs/3/si-apd.eps)

as required to achieve a high quantum efficiency at the shorter wavelengths for which the detector is designed. The avalanche region multiplies the number of electron-hole pairs by a gain (usually in the order of 100) and therefore can produce relatively high output photocurrent compared to conventional PIN photodiodes. In the model discussed in this section we consider TPA process in a slab of silicon of thickness d with infinitely large area. A Gaussian beam incident on this slab generates TPA photocurrent in the detector. First we calculate the total TPA absorbed power in the slab. Figure 3.8 shows a detailed image of the Gaussian beam and the detector. When the beam enters the silicon slab, it undergoes refraction and therefore the beam waist position changes. There can be different situations for solving this problem considering different positions of the beam waist (inside the slab, before or beyond the slab) but one can easily show that the final formula holds for all these situations. Now let us solve the problem for the case that the beam waist is inside the slab. When the Gaussian beam undergoes refraction from air into a medium of refractive index n we can show using Gaussian beam formulation that [2]:

- The distance from the beam waist to the boundary is n times the distance from the beam waist to the boundary if $n = 1$ (see figure 3.8).
- Spot-size of the beam at the beam waist (w_0) does not change by entering the slab.
- Evolution of the spot-size with z follows the same formula as a beam in the air but the confocal parameter z_0 should be multiplied by n.

[2] These statements are shown in Appendix B

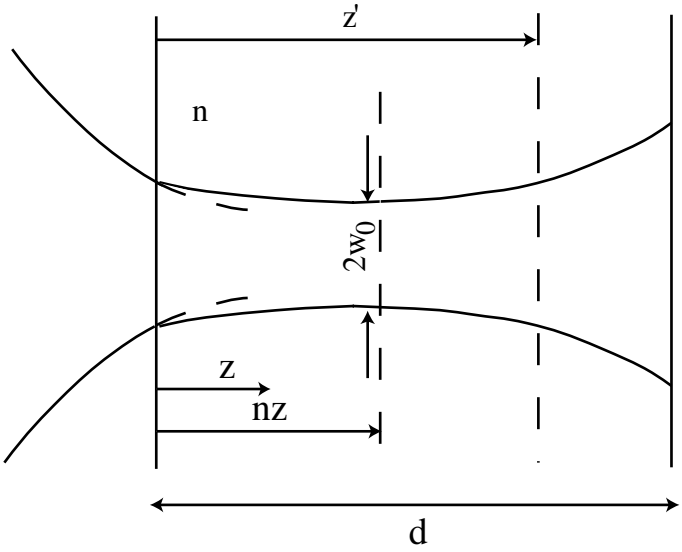

Fig. 3.8: Gaussian beam incident on a slab of silicon. Figure shows the refraction of the beam and the parameters used for the calculations. (figs/3/gauss-slab.eps)

Two-photon absorption coefficient β gives the change in the intensity of light as it travels through the medium:

$$\frac{dI}{dz} = -\beta I^2 \tag{3.13}$$

But β is very small ($\beta I d \ll 1$) and the amount of power that is absorbed is negligible compared to the incident power. Therefore one can assume no variation of the intensity with z. In this case intensity at any point with a distance z' from the front face of the slab and radial distance r from the axis of the beam can be given by:

$$I(r, z') = I_0(z') \exp\left(-\frac{2r^2}{w^2(z')}\right) \tag{3.14}$$

In this equation $I_0(z')$ is the intensity on the axis of the beam at a distance z' from the front face of the slab. $w(z')$ is also the beam radius at this point. According to the assumption that the absorbed power is much smaller than the incident power $I_0(z')$ can be written as:

$$I_0(z') = \frac{2P}{\pi w^2(z')} \tag{3.15}$$

Where P is the power of the incident beam [3]. Also $w(z')$ can be easily written in a form similar to Eq. 3.12 after considering the situation in figure 3.8:

$$w^2(z') = w_0^2 \left[1 + \left(\frac{z' - nz}{nz_0}\right)^2\right] \tag{3.16}$$

Where $z_0 = \frac{\pi w_0^2}{\lambda}$. The power absorbed in a differential slab of thickness dz' can be written as:

$$dP_{abs} = \beta dz' \int_0^\infty I^2(r, z') 2\pi r dr = \frac{1}{4}\beta\pi I_0^2(z') w^2(z') dz' \tag{3.17}$$

Therefore to calculate the total absorbed power one should evaluate the following integral:

$$P_{abs} = \frac{\beta}{\pi} P^2 \int_0^d \frac{1}{w^2(z')} dz' \tag{3.18}$$

Now by substituting from Eq. 3.16 we can evaluate the integral and the final absorbed power will be:

$$P_{abs} = \frac{n\beta}{\lambda}\left[\tan^{-1}\left(\frac{d - nz}{nz_0}\right) + \tan^{-1}\left(\frac{z}{z_0}\right)\right] P^2 \tag{3.19}$$

[3] In fact P is the part of the incident power that is transmitted into the slab.

The absorbed power is a function of z and is maximized when $z = \frac{d}{2n}$. The maximum power through two-photon absorption would be:

$$P_{\text{abs}}^{\max} = \frac{2n\beta}{\lambda} \tan^{-1}\left(\frac{\lambda d}{2\pi n w_0^2}\right) P^2 \tag{3.20}$$

Now let us look at the limiting cases of this maximum power:

- The spot-size is big enough so that the detector can be considered as a very thin slab, mathematically: $z_0 \gg \frac{d}{2n}$. In this case one expects to get the same result of the calculations in section 3.3. By approximating the inverse tangent with its argument we get:

  $$P_{\text{abs}}^{\max} \simeq \frac{\beta d}{\pi} \frac{P^2}{w_0^2} \tag{3.21}$$

  This equation shows that the absorbed power is inversely proportional to πw_0^2 which is the spot area.

- The spot-size is very small and the thickness of the detector is much bigger than the confocal parameter of the beam, mathematically: $z_0 \ll \frac{d}{2n}$. In this case the value of the inverse tangent is approximately $\frac{\pi}{2}$ and we get:

  $$P_{\text{abs}}^{\max} \simeq \frac{n\beta\pi}{\lambda} P^2 \tag{3.22}$$

  This equation shows that for very small spot-sizes the absorbed power has a limit and cannot be further increased by making the spot-size smaller. This is the most

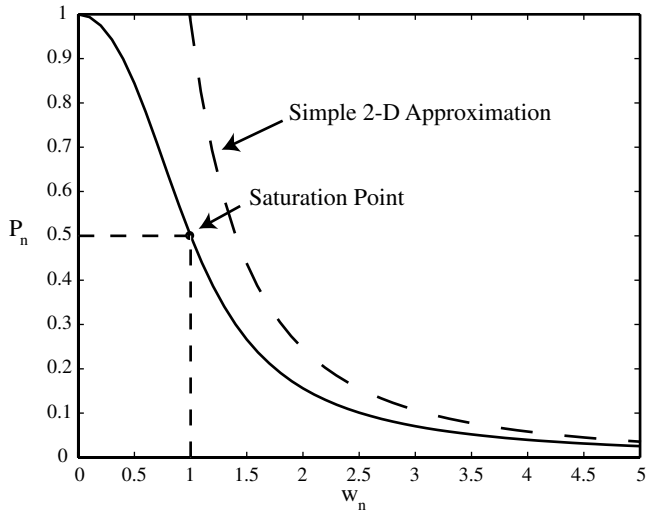

Fig. 3.9: Normalized maximum TPA power vs. normalized spot-size. Tha saturation point and the 2-D approximation are shown. (figs/3/abs-power-curve.eps)

important result of this calculation which indicates a limit for the TPA photocurrent as the spot-size of the beam is decreased.

Finally let us consider the plot of the normalized maximum absorbed power (P_n) vs. the normalized spot-size (w_n). The power is normalized to the value at very small spot-size, $\frac{n\beta\pi}{\lambda}P^2$, and the spot-size is normalized to the value $\sqrt{\frac{\lambda d}{2\pi n}}$. Therefore formula given in Eq. 3.20 can be simplified as : $P_n = \frac{2}{\pi}\tan^{-1}(w_n^{-2})$. The plot is shown in figure 3.9 and shows that making w_0 smaller than a saturation point can only improve the TPA current by at most a factor of 2 which is not anticipated by the two-dimensional model of the problem. The point defined as the saturation point is shown in figure 3.9 and refers to $w_n = 1$ or :

$$w_{0,sat} = \sqrt{\frac{\lambda d}{2\pi n}} \tag{3.23}$$

This formula helps us to find the right spot size for a certain detector assuming that the thickness of the absorption region is known. Also knowing the minimum achievable spot-size we can find the suitable thickness of the intrinsic region which is corresponding to the saturation point shown in figure 3.9:

$$d_{sat} = \frac{2\pi n w_0^2}{\lambda} = \frac{\pi n \lambda}{2(NA)^2} \tag{3.24}$$

In the next section we will provide experimental results that confirms the spot-size dependence of the TPA photocurrent and we will give a rough estimation for the thickness of the absorbing region.

3.6 Spot-size Sensitivity Results

In Eq. 3.19 parameter z can be controlled using the translation stage. As explained before a three-axis translation stage is used to move the detector in x,y,z directions and therefore by movement in the z direction TPA photocurrent should follow a function similar to Eq. 3.19. The stage moves in the z direction with $1\mu m$ steps and since the confocal parameter of the beam z_0 is about $20\mu m$ this stage has sufficient precision for this experiment. A MATLAB program is written that fits the data points of output TPA voltage on the lock-in amplifier and distance z to the formula given in Eq. 3.19. Parameter z is measured with respect to

an arbitrary origin but then in the fitting program the amount of shift is determined. In this program we tried two fitting methods:

1. In the first method, four fitting parameters are used: w_0, d, A (a parameter that included all constants that are multiplied by the output voltage) and D (the shifting parameter that gives the amount of shift for z to get to the right origin). The beam waist w_0 is already known but by this method we can check that the model is acceptable for this type of problem if the calculated w_0 is close to what was independently measured.

2. In the second method we eliminate one of the parameters w_0 and therefore obtain a better estimate of d. But as we will explain later this model may not be an accurate measurement technique to find the thickness of the absorption layer.

Figures 3.10 (a) and (b) show the data and the calculated curves with the MATLAB program for $10\times$ and $20\times$ lenses respectively. The results obtained from the fitting program are summarized in table 3.3, which gives the values of w_0 found by method 1 and d found by method 2 after plugging in the actual spot-size values. Calculation of d has an uncertainty due to different values obtained from different measurements and the reason for having different results will be discussed in Section 3.8 where we see that the surface of the detector does not seem to be uniform. Therefore this value of d just gives the effective thickness of the absorbing layer inside the APD. The results agree with what would be expected based on the vendor-specified quantum efficiency at $\lambda \simeq 1\mu m$ and the linear

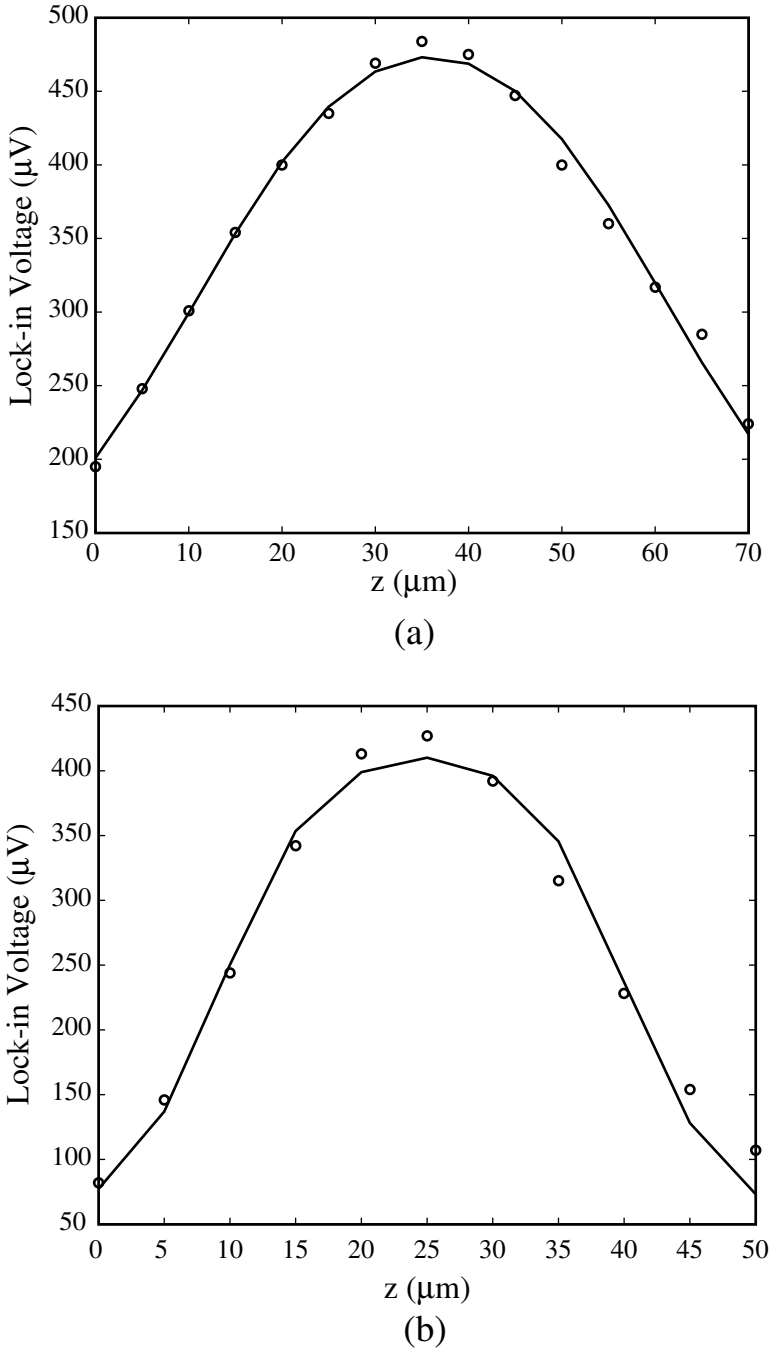

Fig. 3.10: Output voltage of the lock-in amplifier vs. the distance in the z direction for 10× (a) and 20× (b) lenses. The curve calculated from the fitting program is shown. (figs/3/spotsize-result.eps)

Magnification	$\mathbf{w_0}(\mu\mathbf{m})$	$\mathbf{d}(\mu\mathbf{m})$
$10\times$	3.6	120
$20\times$	2.2	100

Tab. 3.3: Measured values of the spot-size and the thickness of the absorption region from fitting Eq. 3.19 to the experimental data

absorption coefficient α at this wavelength.

3.7 Surface Reflection Effect

Most optical detectors have an antireflection coating that is designed to maximize the amount of light delivered to the absorption region. But the antireflection coating works best at one specific wavelength. In order to reduce the reflection of the light incident from air on the surface of a material with refractive index n, one can show using transformation of impedance method [21] that:

- The coating material should have a refractive index of $\sqrt{n}$.
- The thickness of the coating layer should be $\frac{\lambda}{4\sqrt{n}}$ where λ is the wavelength of the light in air.

Because the detector is designed for use at 830 nm wavelength, when used in 1550 nm the reflectivity of the surface is in general non-zero. In this section we give a calculation

of the reflected power from the antireflection coated detector when it is used at a different wavelength.

If λ is the wavelength for which the antireflection coating is designed and λ' is the actual wavelength used, let $t = \dfrac{\lambda'}{\lambda}$ and using the method of impedance transformation we can show:

$$R = \frac{(1-n)^2}{(1+n)^2 + 4n\tan^2(\dfrac{\pi t}{2})} \tag{3.25}$$

where R is the power reflectivity of the surface. In this equation it is easy to observe that for $t = 2$ the value of R approaches the reflectance of a surface without any antireflection coating. Now using Eq. 3.25 we calculated R for a Silicon detector ($n \simeq 3.5$) and $\lambda = 830nm$ and different wavelengths to use on the detector. The calculated power reflectivity is given in table 3.4. The TPA photocurrent that is generated is proportional to square of the transmitted power. The relative values of TPA photocurrent is given for a few different wavelengths in table 3.4. Note that this analysis assumes that the antireflection coating has an index of refraction of $\sqrt{n}$, which can only be approximately achieved in practice. Also, we have assumed that the refractive indices do not vary appreciably with wavelength. This table shows that the TPA photocurrent can be reduced by a factor of 2 because of this reflection which is another sensitivity issue to consider especially in order to make a detector customized for TPA process.

Wavelength (nm)	t	Power reflectivity (%)	Relative TPA (%)
950nm	1.14	2.2	95.6
1100nm	1.32	9.6	81.6
1250nm	1.51	18.5	66.4
1400nm	1.69	25.7	55.1
1550nm	1.87	29.9	49.1

Tab. 3.4: Calculated power reflectivity and relative TPA for different wavelengths used on a silicon detector having an antireflection coating at 830nm.

3.8 Nonuniform Surface of the Detector

In most of the formulas derived in this chapter we assumed that the surface of the detector is uniform enough to assume that the efficiency of the TPA process is uniform over the active area of the detector. But we observed experimentally that there are significant issues with this assumption. In order to look at this problem first we moved the detector in the transversal directions (x and y). The detector's active area is circular shape with a diameter of $500\mu m$ and the beam size at the focal point as mentioned before was about $6\mu m$ for the $10\times$ lens and $4\mu m$ for the $20\times$ lens. These numbers show that a uniform detector should not be sensitive to movements in x and y directions as long as the beam is inside the detector and z is kept constant. However, measurements show a nonuniform response over the area of the detector. Some areas show more uniform response while in other areas local peaks are observed. The results of this experiment are shown in figure 3.11 (a) and (b). In this experiment the beam is scanned along the two main diameters of the detector area in the x and y directions. The translation stage used in this measurement has a limitted travel

of 200 μm, which prevents one from travelling the entire 500 μm diameter in a single scan. The data plotted therefore only cover half of the detector. Results in figures 3.11 (a) and (b) show the TPA output voltage only for the x direction in the two halves of the detector diameter. Also in this figure we plot the single-photon absorption with the 980nm source which shows a uniform result for the single-photon absorption experiment on the exactly same path. The power used for 980nm source is much lower than the 1550nm source but still the output voltage from the single-photon absorption is plotted 3 orders of magnitude lower to be able to be compared with the two-photon absorption voltage. The results shown in this figure are really unexpected especially the fact that linear absorption is uniform over the surface while two-photon absorption is greatly enhanced is some regions. Qualitatively similar results are seen in the y direction.

The first conclusion of this experiment is that the experiment described in Section 3.6 should be done on the areas of the detector that the TPA output is more uniform. In the following subsection we will consider possible explanations for this effect.

3.8.1 Possible Explanations

Following reasons can be considered as different possibilities for this effect:

- **Defects in the detector material** : If the silicon in the detector contains some impurities or defects this may cause a nonuniform pattern similar to what we see in figure 3.11. But looking at the single-photon absorption response of the same path on the

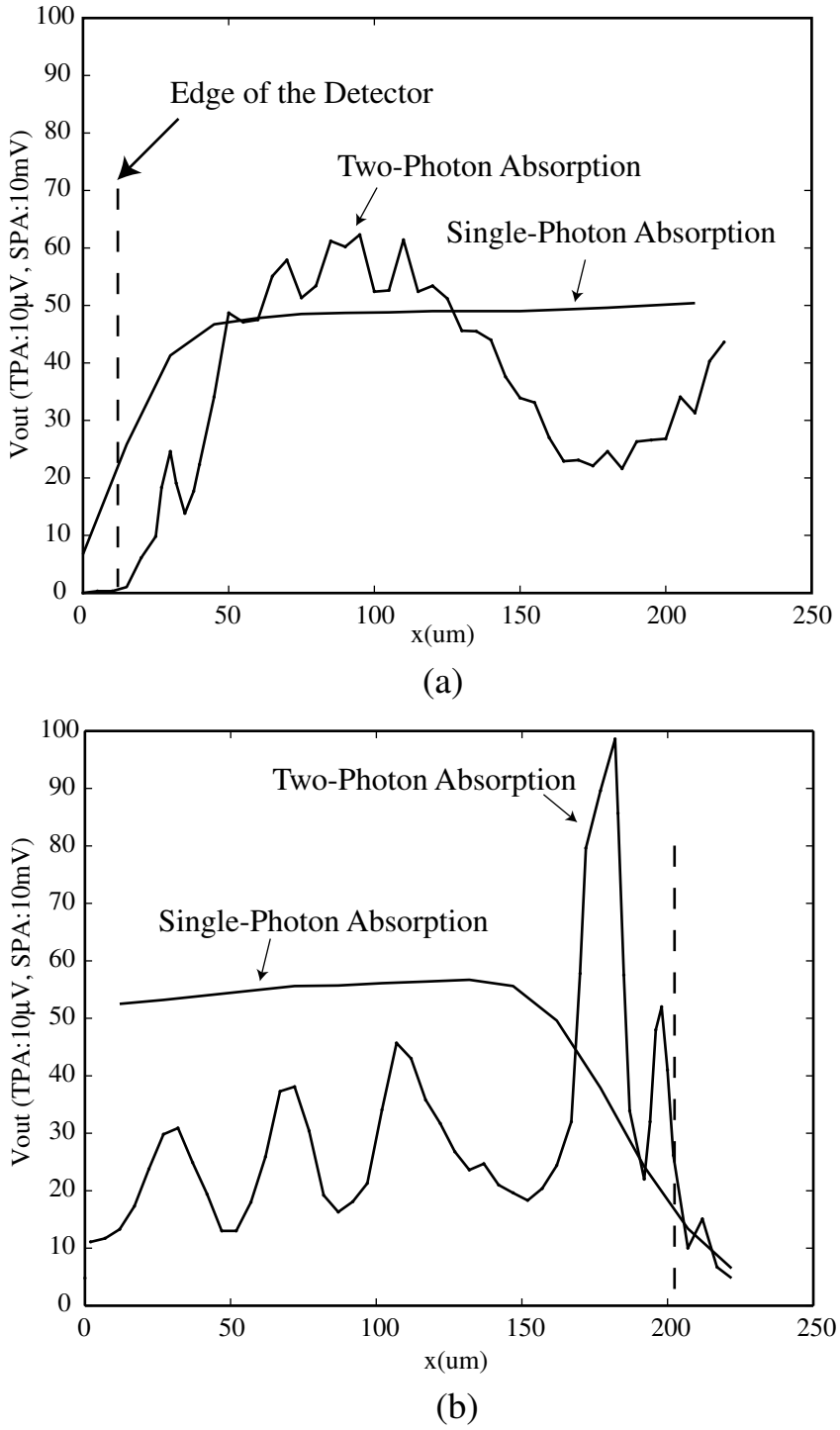

Fig. 3.11: TPA and SPA voltage along the horizontal diameter of the detector. Parts (a) and (b) of the figure show two pieces of this diameter scanned by the beam.

(figs/3/trans.eps)

detector makes this possibility weak since one expects to see the same pattern for this response. Although the defects may effect only the TPA process.

- **Reflection from the surface of the detector** : This assumption is based on the fact that some light gets reflected from the glass window or the silicon surface. The reflection from the glass is about 5% and from the silicon is about 30% which can not make any effect similar to figure 3.11. If we assume that the antireflection coating does not work for 1550nm wavelength, this is something that distinguishes between the SPA and TPA processes but can explain only a few percent variation in the transversal plain.

- **Reflection from the back surface** : This possibility is the strongest since it completely separates the cases of a 980 nm and 1550 nm wavelengths. The absorption coefficient of the detector at 980 nm wavelength is much higher than at 1550 nm wavelength, therefore the intensity of 980 nm light decays much faster than 1550 nm light when it enters the detector. Figure 3.12 shows the typical decay rate of the optical power for 980 nm and 1550 nm signals passing through a slab of silicon. Therefore the reflection on the back surface should not have any effect on the 980 nm light whereas the effect on 1550 nm can be significant. In some devices a metal contact is deposited on the back surface and this makes a highly-reflective surface for the light. Now if this surface has some roughness or irregularity due to fabrication issues it might cause the nonuniform pattern similar to fig 3.11. This nonuniform response could be caused by some complex interference effect.

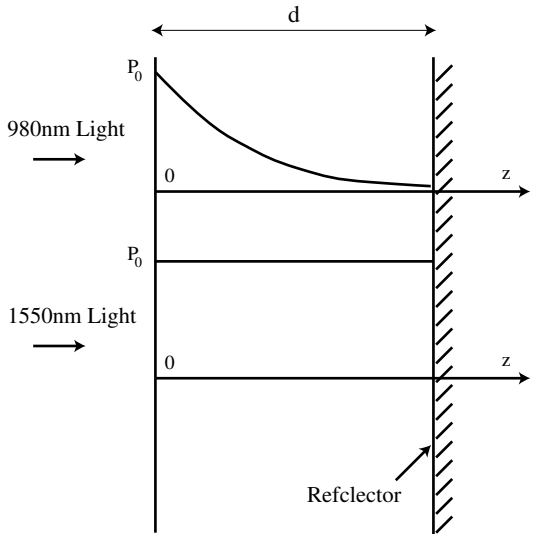

Fig. 3.12: Decay of power for 980nm and 1550nm light entering a slab of silicon. Figure shows how the power of the 980nm decays faster. (figs/3/decay.eps)

3.8.2 Explanation of the Nonuniform Response

After discussing 3 possible explanations for what causes the nonuniform response of the detector, reflection from the back surface seems most likely to be the real cause of this irregular response. In order to confirm this explanation, we did another measurement in which we vary the wavelength of the light around 1550 nm. If the cause of this nonunifromity is some interference effect we expect to see variations in the output by sweeping the wavelength. Figure 3.13 shows the response of the detector when the light is focused on a fixed point of the detector as the wavelength of the input light is changed. As we clearly see in figure 3.13, the TPA photocurrent changes by a factor of about 5 as we go from a peak to a minimum. This experiment proves that some interference effect occurs in the device.

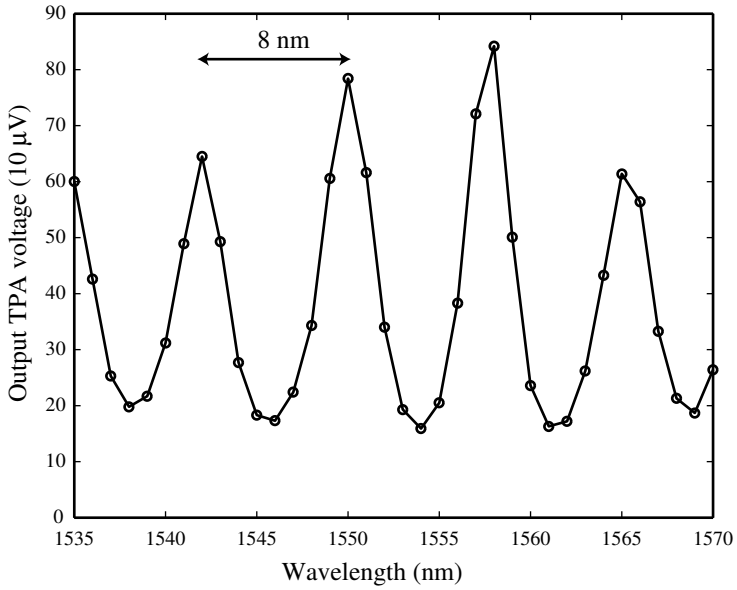

Fig. 3.13: TPA output voltage vs. the input light wavelength. (figs/3/wavelength.eps)

The other observation is that the peaks are spaced evenly and the wavelength difference between them is about 8 nm in the wavelength domain, which corresponds to 1000 GHz in the frequency domain. This observation gives an idea about what could be happening in the device. In a Fabry-Perot interferometer the same frequency dependence can be observed. The peaks of the reflected or transmitted light in a Fabry-Perot interferometer are spaced evenly in frequency domain (or approximately evenly in wavelength domain). If the distance between the two plates in a Fabry-Perot interferometer changes, the locations of the peaks and minimums in the wavelength domain shifts depending on the amount of change in the distance. Now assume that the back surface of the detector (which is possibly a metal contact) has irregularities such as not being parallel to the front surface in some areas or

roughness. In this case the distance between Fabry-Perot plates (or their angle) changes and this can make significant variations in the places of peaks and minimums and therefore cause the nonuniform pattern such as what we see in figure 3.11. In order to confirm this we moved the detector in the transverse direction from a maximum to a minimum and then tuned the wavelength in the minimum so that we get the same output of the maximum point. This was done at a few points on the detector and each time we were able to adjust the wavelength to get a relatively flat response instead of the nonuniform response that is shown in figure 3.11. In the next section we will give a simple analysis of this assumption.

3.8.3 Fabry-Perot Model

In this section we consider a simplified model for the reflection from the back surface of the detector. As mentioned in Section 3.8.1 the intensity of the light for a TPA process does not decay significantly as it goes through the slab of silicon in the device. This is because of the fact that β, the TPA coefficient, for silicon is about 2 cm/GW and therefore the parameter $\beta I d$ is very small for this thickness of the device. Therefore in order to analyze the problem we will assume no attenuation in the electromagnetic fields propagation in the medium. In figure 3.14 4 propagating waves are shown. E_i is the amplitude of the electric field of the incident light propagating in the direction of the z axis and E_r is the amplitude of the reflected light into the air travelling in the opposite direction of the z axis. E_f and E_b indicate the amplitudes of the forward and backward waves inside the medium. Now to analyze the problem we have to write the boundary conditions at the two boundaries. The

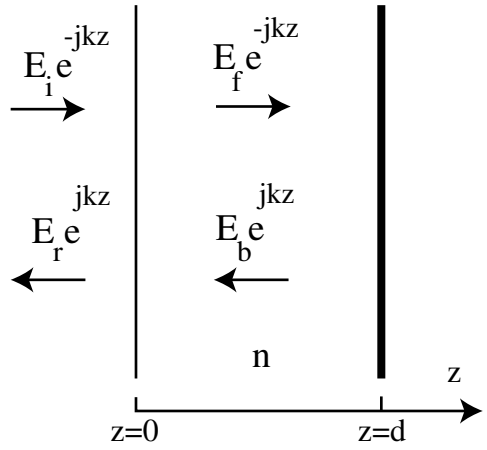

Fig. 3.14: Simple Fabry-Perot analysis for the reflection from the back surface of the detector. (figs/3/fp.eps)

assumptions are:

- All waves are plane waves.
- The reflection coefficient of the front surface is r_1 and the reflection coefficient of the back surface is r_2. The transmission coefficient from the air into the medium is t_1.
- There is no loss inside the medium.

The boundary conditions required for solving the problem are:

$$\begin{aligned} E_f &= t_1 E_i + r_1 E_b \\ E_b e^{jkd} &= r_2 E_f e^{-jkd} \end{aligned} \tag{3.26}$$

where $k = \frac{2\pi n}{\lambda}$ is the wave constant. Solving these two equations for $|E_f|$ and $|E_b|$ gives:

$$\begin{aligned} |E_f| &= \left| \frac{t_1 E_i}{1 - r_1 r_2 e^{-j2kd}} \right| \\ |E_b| &= |r_2||E_f| \end{aligned} \tag{3.27}$$

The electric field inside the medium is the summation of the forward and backward fields and since $|E_b| = |r_2||E_f|$, the two-photon absorption photocurrent generated in the medium should be proportional to $|E_f|^4$:

$$i = K|E_f|^4 \tag{3.28}$$

where K is a proportionality constant [4]. substituting this in Eq. 3.28 and simplifying we obtain the following equation for the output photocurrent:

$$i(d) = K \frac{|t_1|^4}{|1 - r_1 r_2 e^{-j2kd}|^4} |E_i|^4 \tag{3.29}$$

From this equation one can easily see that the maximum and minimum values of the photocurrent are:

$$\begin{aligned} i_{\max} &= K \frac{|t_1|^4}{(1 - |r_1||r_2|)^4} |E_i|^4 \\ i_{\min} &= K \frac{|t_1|^4}{(1 + |r_1||r_2|)^4} |E_i|^4 \end{aligned} \tag{3.30}$$

[4] since $|E_b| = |r_2||E_f|$, K depends on $|r_2|$

If k changes by $\Delta k = \frac{\pi}{d}$, the photocurrent does not change. Therefore the difference between the wavelengths of the peaks in figure 3.13 is:

$$\Delta\lambda \simeq \frac{\lambda^2}{2nd} \tag{3.31}$$

Using figure 3.13 we can substitute $\Delta\lambda = 8\,nm$ and we get $d \simeq 43\,\mu m$. This value of d is reasonable according to design considerations discussed is Section 3.5 but is different from the value found in this section because the models are different. In fact the amount of d found before is the effective d which is more than the actual d. In figure 3.15 we have plotted the relative photocurrent $\left(\frac{i}{i_{\max}}\right)$ as a function of wavelength for the same range of wavelength in the experiment and the amount of d found from figure 3.13. Now let us give some numerical values for $|r_1|$ and $|r_2|$. Calculation of $|r_1|$ is based on the equation given in Section 3.7 where we discussed the existence of an antireflection coating on the surface of the detector. If we assume that the material used for this coating is silicon nitride with refractive index of about 2 and the detector is designed for the wavelength of 830 nm, then $|r_1| \simeq 0.4$. The value of $|r_2|$ depends on the structure of the detector. If we assume that the back of the detector is coated with a metal contact we can assume that $r_1 \simeq 1$. In order to compare this theoretical result with out results we calculate the ratio between the maximum and minimum output photocurrents:

$$\frac{i_{\max}}{i_{\min}} = \left(\frac{1+|r_1||r_2|}{1-|r_1||r_2|}\right)^4 \tag{3.32}$$

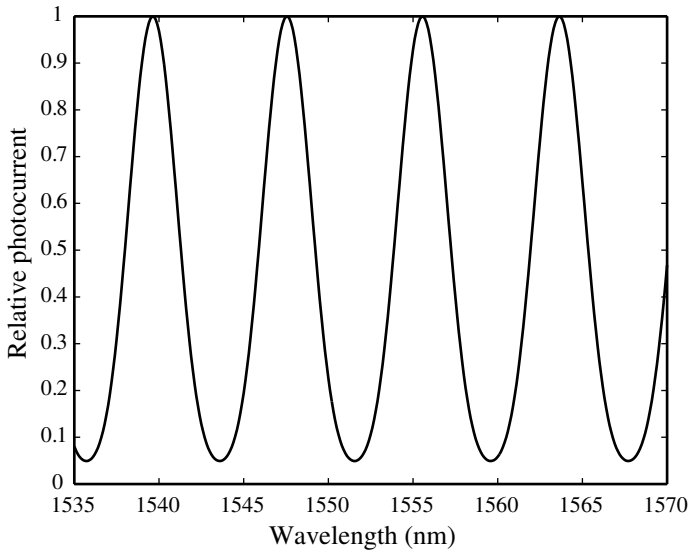

Fig. 3.15: Theoretical plot of the TPA photocurrent vs. wavelength for a simple FP model. (figs/3/fp-theory.eps)

By substituting $r_1 = 0.4$ we get:

- $\frac{i_{\max}}{i_{\min}} \simeq 30$ for $r_2 = 1$
- $\frac{i_{\max}}{i_{\min}} \simeq 20$ for $r_2 = 0.9$
- $\frac{i_{\max}}{i_{\min}} \simeq 14$ for $r_2 = 0.8$

Therefore depending on what the value of the reflection coefficient is the ratio between the maximum and minimum values of the photocurrent can change significantly. Now if we look at figure 3.13 this ratio is about $\frac{i_{\max}}{i_{\min}} \simeq 5$. Even with a low reflectivity of 0.8 for the back surface we get 3 times bigger value for the ratio between the maximum and minimum values of the photocurrent.

We believe that the discrepancy arises because the simple Fabry-Perot analysis described here assumes that the field is a plane wave, whereas in our experiment a focused beam was used. The beam has a full divergence angle of about $\theta \simeq \sin^{-1}(NA) = 24^o$ for the $10\times$ lens. So multiple reflections from the boundaries will not have a complete overlap with each other as a plane wave model assumes. This may be the main reason for getting a different numerical value. Another possible explanation is that the back surface may not be completely flat or smooth and therefore the reflection coefficient from this surface may be lower than what we have assumed.

3.8.4 Conclusions from the Fabry-Perot model

The results of this analysis on the nonuniform response of the detector can be summarized as:

1. The Fabry-Perot model can explain the nonuniform response of the detector.

2. Based on this analysis one can estimate the thickness of the absorbing region of the detector.

3. In order to fabricate customized detectors for TPA process one important consideration would be choosing the right antireflection coating on the front surface of the detector to reduce r_1 as much as possible.

4. The other consideration in fabricating detectors would be depositing absorptive ma-

terials to the 1550 nm light on the back of the actual absorption region which can reduce r_2.

3.9 Bias Voltage Sensitivity

The last parameter we considered in this chapter is the effect of the bias voltage in the detector. In an APD the bias voltage changes the avalanche gain (M) of the detector. The reverse biased detector is very close to breakdown and as the bias voltage gets closer to the breakdown voltage, M increases. For the TPA process we observed the same behavior that is expected because the bias voltage should not have a significant effect on the absorbed power and only changes the avalanche gain. Figure 3.16 shows output voltage vs. input power for the TPA process under three different bias voltages.

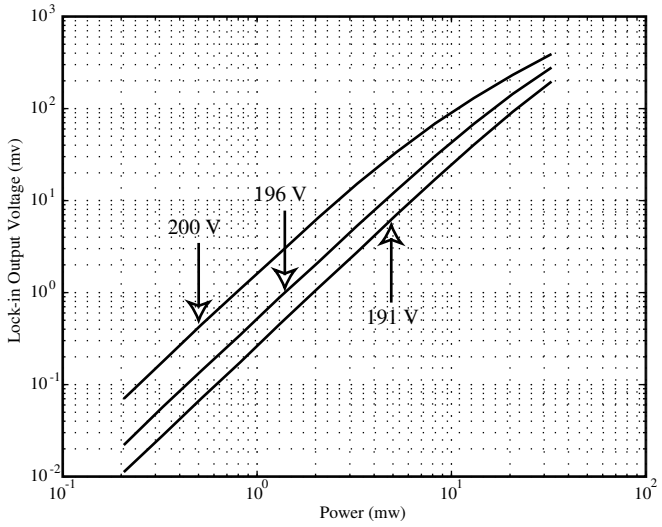

Fig. 3.16: TPA output voltage vs. input power for different bias voltages. (figs/3/bias.eps)

4. POLARIZATION SENSITIVITY

In the last chapter we discussed most of the parameters that can change the TPA photocurrent of the detector and gave experimental results. In this chapter another parameter is introduced which falls into a different category and therefore is discussed separately. In a regular detector with single-photon absorption which is made of an isotropic material, there is no change in the detected photocurrent when the light polarization changes. In other words as long as the power of the beam is constant, the polarization of light does not have any effect on the output current. But in a TPA process as we will show in this chapter, theoretically and experimentally, changing the polarization from linear to circular can change the photocurrent by a factor of 1.5. This is due to the nonlinear nature of the process, not any anisotropy in the detector material.

4.1 Rotation of linearly polarized light

First to make sure that the detector does not have any axis along which it enhances the TPA process, we rotated the polarization of linearly polarized light. The method of rotation of polarization is simply shown in figure 4.1 (a). In this method first a polarization controller

shown in figure 3.1 is adjusted to get the maximum power out of the polarizer. The linearly polarized light coming out of the polarized enters a half waveplate ($\frac{\lambda}{2}$ plate) that rotates the orientation of the polarization. The power of the light incident on the detector does not change by rotating the waveplate and the polarization stays purely linear.

The principle of operation of such a waveplate is shown in figure 4.1 (b). The plate has a slow and a fast axis. The permittivity of the medium is higher for the electric field along the slow axis than the fast axis. The thickness of the plate is designed in a way that the component of the electric field along the fast axis will have a positive phase shift of π with respect to the component along the slow axis after they pass through the half waveplate. In figure 4.1 the xy coordinate is fixed to the fast and slow axes and the electric field $\mathbf{E}_{in}(t) = E_0 \cos(\theta)\cos(\omega t)\hat{x} + E_0 \sin(\theta)\cos(\omega t)\hat{y}$ makes an angle of θ with the fast axis. The angle θ is the rotation angle of the quarter waveplate which is measurable with a precision of 1 degree. Therefore the electric field coming out of the quarter waveplate can be written as:

$$\mathbf{E}_{\text{out}}(t) = E_0 \cos(\theta)\cos(\omega t)\hat{x} - E_0 \sin(\theta)\cos(\omega t)\hat{y} \tag{4.1}$$

Now if we assume that there is no enhancement along a certain axis for TPA process (i.e. the medium is isotropic) we can write:

$$i_{\text{TPA}} = K \left\langle |\mathbf{E}_{\text{out}}(t)|^4 \right\rangle \tag{4.2}$$

Where K is a constant, i_{TPA} is the TPA photocurrent and $\langle \cdot \rangle$ is time average operator. The

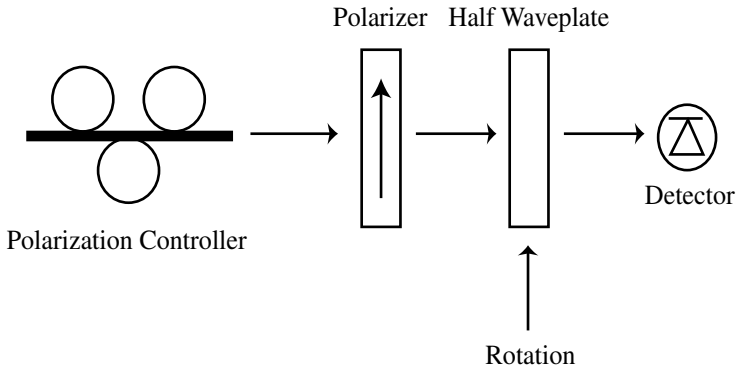

(a)

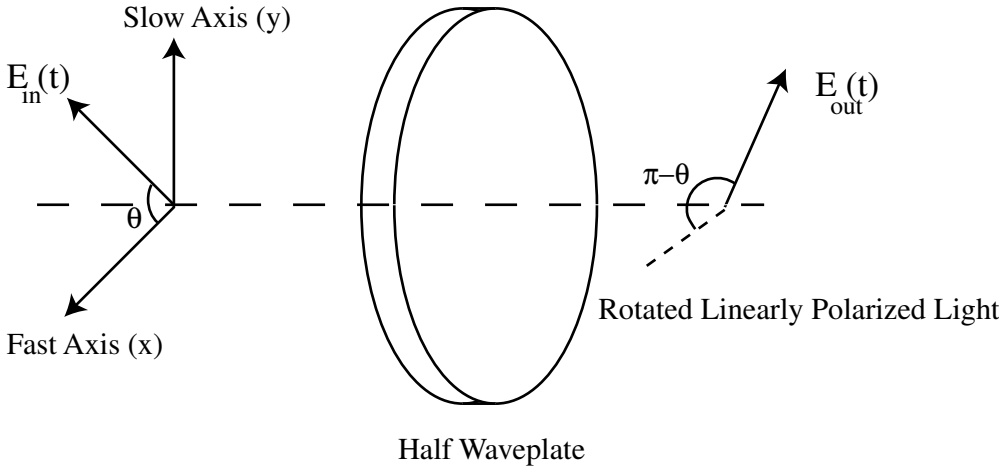

(b)

Fig. 4.1: Schematic of the setup used to generate and rotate linearly polarized light.
(figs/4/lin-pol.eps)

time average operator is to eliminate high optical frequency and can be thought of as a low-pass filter. Now substituting from Eq. 4.1 into Eq. 4.2 we can easily show that:

$$i_{\mathrm{TPA}} = \frac{3K}{8} {E_0}^4 \tag{4.3}$$

Where we have used the formula:

$$\left\langle \cos^4(\omega t) \right\rangle = \frac{3}{8} \tag{4.4}$$

Eq. 4.3 shows the fact that for a linear polarization TPA power is constant as we rotate the polarization by changing θ. Experiment shows that rotating the polarization direction of a linearly polarized light does not have any effect on the TPA photocurrent generated in the detector. Also we checked that 980 nm light (SPA) gives the same result, as expected. This experiment shows that there is no certain axis on the detector that enhances or reduces the TPA process for the light polarized along that axis. This suggest that silicon behaves as an isotropic medium in this detector. As we will see in the next chapter, the nonlinear nature of the process distinguishes between a circularly polarized light and a linearly polarized light even if the medium is isotropic.

4.2 Effect of Elliptically Polarized Light

Now to see the effect of elliptically polarized light we use the setup shown in figure 4.2 (a) which is similar to the setup used in the last section. In this measurement we replace the half waveplate with a quarter waveplate. Rotation of this quarter waveplate gives a phase difference between x and y components of the electric field. The principle of operation of the quarter waveplate is shown in figure 4.2 (b). Similar to the half waveplate, the quarter waveplate has a fast and a slow optical axes. The permittivity of the medium is higher for the electric field along the slow axis than the fast axis. The thickness of the plate is designed in a way that the component of the electric field along the fast axis will have a positive phase shift of $\frac{\pi}{2}$ with respect to the component along the slow axis after they pass through the quarter waveplate. Orientation of the input electric field in figure 4.3 (b) is similar to what was explained for the half waveplate. Therefore the electric field coming out of the quarter waveplate can be written as:

$$\mathbf{E}_{\text{out}}(t) = E_0 \cos(\theta) \cos(\omega t)\hat{x} + E_0 \sin(\theta) \sin(\omega t)\hat{y} \tag{4.5}$$

This equation shows that the output light is:

- Linearly polarized along the x axis for $\theta = m\pi$.
- Circularly polarized for $\theta = (2m+1)\frac{\pi}{4}$.
- Linearly polarized along the y axis for $\theta = (2m+1)\frac{\pi}{2}$.

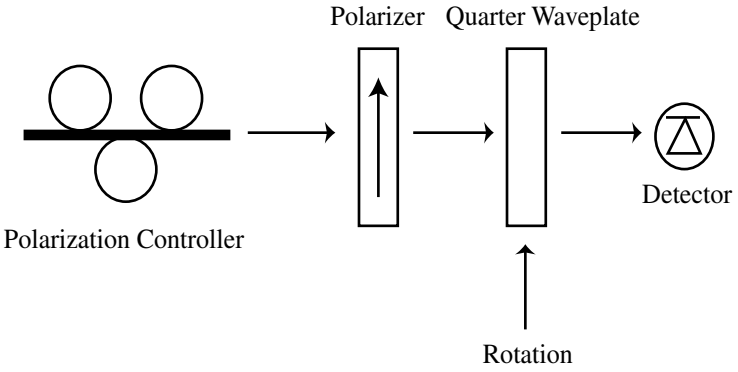

(a)

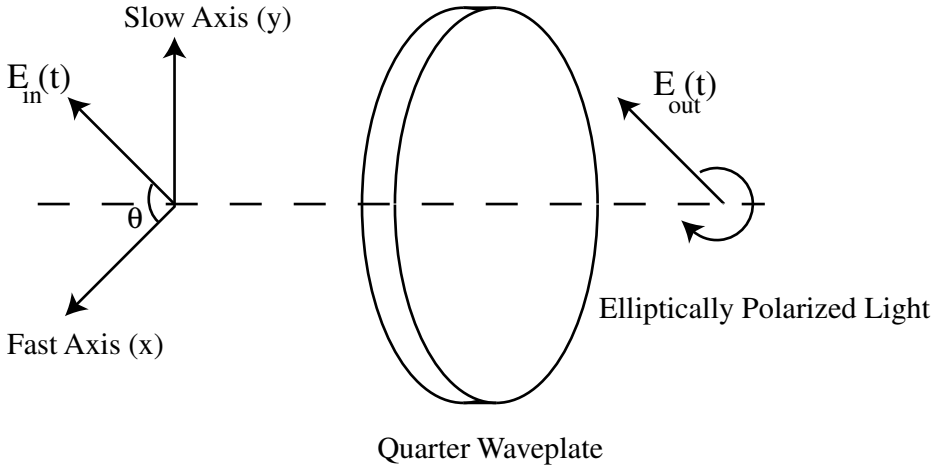

(b)

Fig. 4.2: Schematic of the setup used to generate and control elliptically polarized light. (figs/4/ellip-pol.eps)

- Elliptically polarized for any other value of θ.

Where m is an integer. Based on this formula and and using Eq. 4.2 we can find the TPA photocurrent generated by the wave coming out of the quarter waveplate:

$$i_{\mathrm{TPA}} = K \left\langle |\mathbf{E}_{\mathrm{out}}(t)|^4 \right\rangle = \frac{K}{16} {E_0}^4 \left(5 + \cos(4\theta)\right) \tag{4.6}$$

In this equation we have used Eq. 4.4 along with these similar formulas:

$$\left\langle \sin^4(\omega t) \right\rangle = \frac{3}{8} \tag{4.7}$$

$$\left\langle \cos^2(\omega t) \sin^2(\omega t) \right\rangle = \frac{1}{8} \tag{4.8}$$

Eq. 4.6 shows that in case of an elliptically polarized light, TPA photocurrent is expected to change as a function of the rotation angle θ. This function is periodic with a period of $\frac{\pi}{2}$. The minimum of the TPA power occurs when the light is circularly polarized ($\theta = (2m+1)\frac{\pi}{4}$) and the maximum occurs when the light is linearly polarized ($\theta = m\frac{\pi}{2}$). The ratio between these two values is:

$$\frac{i_{\mathrm{TPA}}(\mathrm{lin})}{i_{\mathrm{TPA}}(\mathrm{cir})} = \frac{3}{2} \tag{4.9}$$

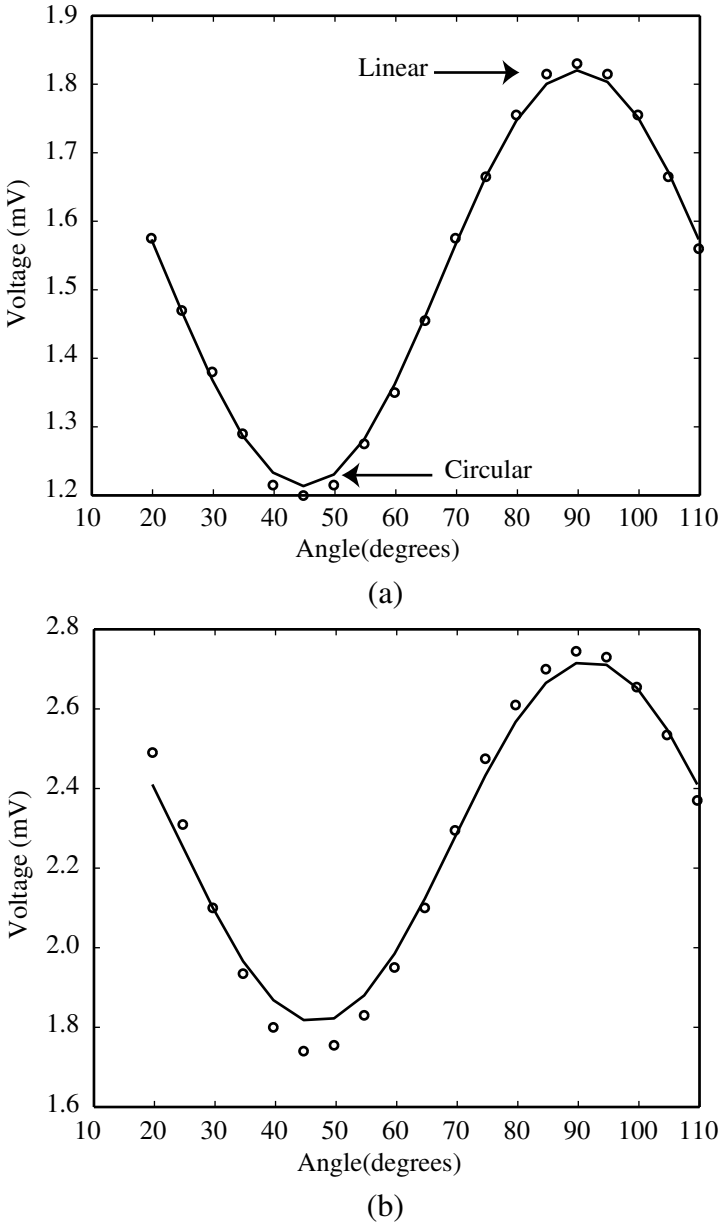

Fig. 4.3: TPA voltage vs. rotation angle of the quarter waveplate. (figs/4/ellip.eps)

Based on the formula given in Eq. 4.6 we can give the formula for the two-photon absorption coefficient (β):

$$\beta(\theta) = \beta_0 \left(\frac{5 + \cos(4\theta)}{6} \right) \tag{4.10}$$

Where β_0 is the absorption coefficient for linear polarization. Now we can compare the experimental results of this part with Eq. 4.6. A MATLAB program is used to fit the data taken from the experiment to Eq. 4.6. The theoretical result (from the MATLAB program) and the experimental data are plotted in figure 4.3 (a) for one period. In figure 4.3 (b) the data from the same experiment is shown when the input electric field is rotated by 90 degrees. In this figure the angle θ does not start from zero and this is because the fast and slow angles of the quarter waveplate are not defined on the plate. Therefore we plotted the data for one period (90^o) and in the MATLAB program we found the shift in the angle. The main result of this experiment is that in a TPA process change in the polarization state of the input light can change the photocurrent by a factor of 1.5 which is a significant factor. Because of this effect in any TPA experiment we need to keep all the fibers taped down and fixed to the optical table. Movement of optical fibers can change the polarization of light and therefore vary the output TPA photocurrent.

4.3 Poincare Sphere Representation

To analyze the polarization of light Poincare sphere representation is usually used. The electric field can be considered as $\mathbf{E}(t) = A_x \cos(\omega t)\hat{x} + A_y \cos(\omega t + \phi)\hat{y}$ or in phaser

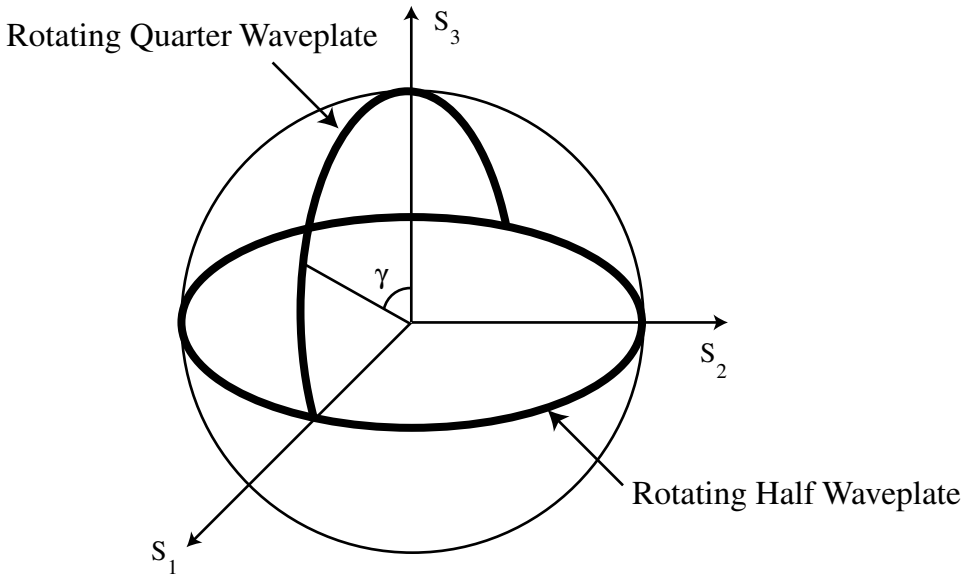

Fig. 4.4: Poincare Sphere representation. (figs/4/poincare.eps)

form as $\underline{\mathbf{E}} = E_x\hat{x} + E_y\hat{y} = A_x\hat{x} + A_y e_{j\phi}\hat{y}$. In the case considered in section 4.2 we have $A_x = E_0\cos(\theta)$ and $A_y = E_0\sin(\theta)$ and $\phi = \frac{\pi}{2}$. Now first consider Stokes parameters defined as [22]:

$$\begin{aligned} S_0 = |E_x|^2 + |E_y|^2 \ , \ S_1 = |E_x|^2 - |E_y|^2 \\ S_2 = 2\mathsf{Re}(E_x E_y^*) \ , \ S_3 = 2\mathsf{Im}(E_x E_y^*) \end{aligned} \tag{4.11}$$

It can be easily verified from Eq. 4.12 that $S_0^2 = S_1^2 + S_2^2 + S_3^2$. Therefore if we look at the coordinate system shown in figure 4.4 (S_1, S_2, S_3) is on a sphere as long as the power

of the light is constant. Substituting the electric field in Eq. 4.12 will give:

$$\begin{aligned} S_0 = |A_x|^2 + |A_y|^2 \ , \ \ S_1 = |A_x|^2 - |A_y|^2 \\ S_2 = 2A_xA_y\cos(\phi) \ , \ \ S_3 = 2A_xA_y\sin(\phi) \end{aligned} \tag{4.12}$$

In this sphere $(S_1, S_2, S_3) = (0, 0, S_0)$ and $(S_1, S_2, S_3) = (0, 0, -S_0)$ correspond to circular polarization and the circle in $S_3 = 0$ corresponds to linear polarization. The rotation of the linear polarization which was done in section 4.1 is equivalent to move around this circle (Shown in figure 4.4). Also rotating the quarter waveplate for 90 degrees is equivalent to moving on the path shown in figure 4.4. We can easily show if γ is the angle between the position vector of any point on the sphere and S_3 axis (shown in figure 4.4), then the two-photon absorption coefficient can be written as:

$$\beta(\gamma) = \beta_0 \left(\frac{5 - \cos(2\gamma)}{6} \right) \tag{4.13}$$

The foregoing analysis can accurately predict the polarization dependence of the TPA for noncrystalline, isotropic materials in which the origin of the nonlinearity is electronic [1] in nature. Examples of such materials are glass, liquids and gasses. However, silicon is a crystalline material, and therefore an accurate treatment of the TPA in silicon requires that we use the full $\chi^{(3)}$ susceptibility tensor.

[1] This is explained more in the next Section

4.4 General Treatment of the Polarization Dependence

This analysis in more general than the analysis given for the isotropic material but assumes that the material is either isotropic or a cubic crystal with $m3m$, $\bar{4}3m$ or 432 symmetry. This assumption is equivalent to assuming that the third-order susceptibility tensor is of the form given in table 2.3. The difference between isotropic and anisotropic material in this case is that for an isotropic material:

$$\chi_{1111} = \chi_{1122} + \chi_{1212} + \chi_{1221} \ , \ (1, 2 = x, y, z) \tag{4.14}$$

where we have eliminated the superscript (3). But this relationship is not true for an anisotropic crystal and we can introduce a new parameter as the anisotropy factor [2]:

$$\sigma = \frac{\chi_{1111} - (2\chi_{1212} + \chi_{1221})}{\chi_{1111}} \tag{4.15}$$

where we have used $\chi_{1122} = \chi_{1212}$ according to Eq. 2.20. This factor is zero for an isotropic medium and can be estimated based on quantum mechanics for some materials. The numerical value of σ calculated for two zincblende semiconductor materials are given in table 4.1 [2]. We were not able to find this number for silicon but the analysis gives an idea about how anisotropy can cause polarization dependence in the TPA process.

In order to find the expression for β we go back to Eq. 2.21 and by expanding the

Semiconductor	Anisotropy Factor
GaAs	-0.62
CdTe	-0.47

Tab. 4.1: anisotropy factor for two zincblende semiconductors [2]

summation and writing three components of the polarization vector we can write:

$$\mathbf{P}^{\mathrm{NL}} = 3\epsilon_0 \left[2\chi_{1212} \left(\mathbf{E} \cdot \mathbf{E}^* \right) \mathbf{E} + \chi_{1221} \left(\mathbf{E} \cdot \mathbf{E} \right) \mathbf{E}^* + \sigma \chi_{1111} \sum_i |E_i|^2 E_i \hat{i} \right] \tag{4.16}$$

where $i = x, y, z$ and $\mathbf{E}$ is the electric field vector of a wave propagating in the direction of a unit vector $\hat{\eta}$ such that $\hat{\eta} \cdot \mathbf{E} = 0$. If η is the coordinate in the direction of propagation (which need not be x, y or z), we can write $\mathbf{E}(\eta) = \mathbf{A}(\eta) e^{-jk\eta}$ and Eq. 2.26 can be written as:

$$\frac{d^2\mathbf{E}(\eta)}{d\eta^2} + \frac{n^2\omega^2}{c^2}\mathbf{E}(\eta) = -\mu_0\omega^2\mathbf{P}^{NL}(\eta) \tag{4.17}$$

Using Eq. 4.16, Eq. 4.17 and equations similar to Eq. 2.32 and Eq. 2.33 we can obtain the following equation:

$$\frac{\partial I(\eta)}{\partial \eta} = -\frac{3\omega}{2\epsilon_0 n^2 c^2} \left[2\mathsf{Im}(\chi_{1212}) + \mathsf{Im}(\chi_1 221) \frac{|\mathbf{A} \cdot \mathbf{A}|^2}{|\mathbf{A}|^4} + \sigma \mathsf{Im}(\chi_{1111}) \frac{\sum_i |A_i|^4}{|\mathbf{A}|^4} \right] I^2(\eta) \tag{4.18}$$

By introducing the unit vector $\hat{p} = \dfrac{\mathbf{A}}{|\mathbf{A}|}$ which is the unit vector representing the polariza-

tion state we can write the TPA coefficient for the medium:

$$\beta = \frac{3\omega}{2\epsilon_0 n^2 c^2}\left[2\mathsf{Im}(\chi_{1212}) + \mathsf{Im}(\chi_{1221})\left|\hat{p}\cdot\hat{p}\right|^2 + \sigma\mathsf{Im}(\chi_{1111})\sum_i |p_i|^4\right] \tag{4.19}$$

This formula is given in [2]. Unit vector $\hat{p}$ can be complex, to accommodate circular and elliptical states, provided that $\hat{p}\cdot\hat{p}^* = 1$. Now based on this formula we can consider some special cases:

1. **Isotropic medium, linearly polarized light**: First let us consider the case of an isotropic medium and compare the results from this equation with the analysis we did before. For this case $\sigma = 0$ and if the light is linearly polarized we have $\hat{p}\cdot\hat{p} = 1$ which gives us:

$$\beta = \frac{3\omega}{2\epsilon_0 n^2 c^2}\left(2\mathsf{Im}(\chi_{1212}) + \mathsf{Im}(\chi_{1221})\right) = \frac{3\omega}{2\epsilon_0 n^2 c^2}\mathsf{Im}(\chi_{1111}) \tag{4.20}$$

   This gives us the same as that obtained in Eq. 2.35 and shows no polarization dependence for the linearly polarized light.

2. **Isotropic medium, circularly polarized light**: In this case we have $\hat{p} = \frac{1}{\sqrt{2}}\hat{x} + \frac{j}{\sqrt{2}}\hat{y}$ and therefore $\hat{p}\cdot\hat{p} = 0$ and the TPA coefficient is:

$$\beta = \frac{3\omega}{\epsilon_0 n^2 c^2}\mathsf{Im}(\chi_{1212}) \tag{4.21}$$

   Different physical mechanisms may lead to the nonlinear susceptibility. In the case

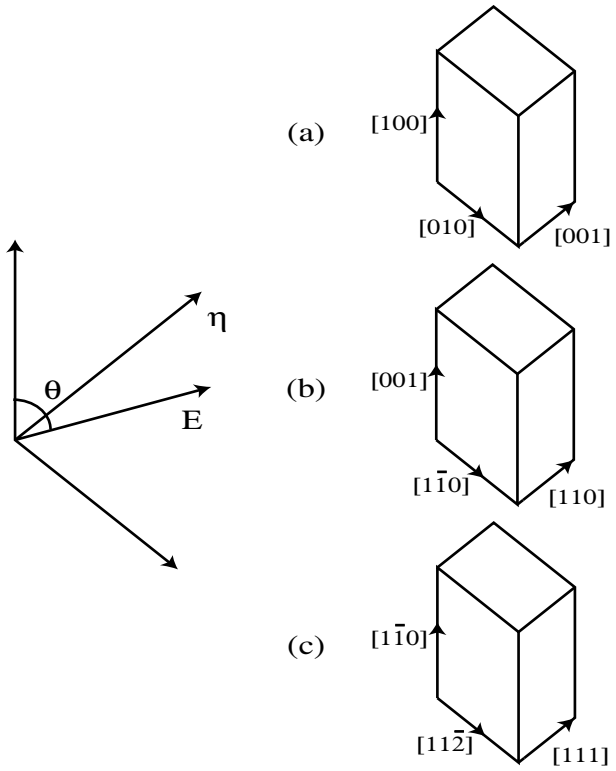

Fig. 4.5: Different cuts of the cubic crystal and the relative orientation of the electric field with respect to crystal axis. (figs/4/crystal.eps)

of the semiconductor materials the most important mechanism is the non-resonant electronic response which provides $\chi_{1221} = \chi_{1212}$ [1]. Using this condition we can see that:

$$\frac{\beta_{\text{lin}}}{\beta_{\text{cir}}} = \frac{3}{2} \tag{4.22}$$

which is the result that we got from the simple analysis in Section 4.2.

3. **Anisotropic cubic crystal**: For the certain class of cubic crystals that we analyze in this section, depending on the type of the crystal cut three cases can happen [2]:

- **Crystal cut perpendicular to [100] direction, linearly polarized light**: In this case figure 4.5 (a) shows the orientation of the electric field and the crystal axis. From the figure one can easily see that $\hat{p} = \cos(\theta)\hat{x} + \sin(\theta)\hat{y}$ for a linearly polarized light rotated by an angle θ with respect to [100] axis (see figure 4.5). Using Eq. 4.19 we can show that:

$$\beta(\theta) = \frac{3\omega}{2\epsilon_0 n^2 c^2}\mathsf{Im}(\chi_{1111})\left(1 - \frac{\sigma}{2}\sin^2(2\theta)\right) \tag{4.23}$$

and this shows a change in the TPA coefficient by rotating the direction of the linearly polarized light.

- **Crystal cut perpendicular to [110] direction, linearly polarized light**: This case is shown in figure 4.5 (b) and from this figure for a linear polarization we have [2] $\hat{p} = \frac{\sin(\theta)}{\sqrt{2}}(\hat{x} - \hat{y}) + \cos(\theta)\hat{z}$. Substituting this in Eq. 4.19 gives us TPA coefficient as a function of θ:

$$\beta(\theta) = \frac{3\omega}{2\epsilon_0 n^2 c^2}\mathsf{Im}(\chi_{1111})\left[1 - \frac{\sigma}{2}(1 + 3\cos^2\theta)\sin^2\theta\right] \tag{4.24}$$

In this case also, we see a change in the TPA coefficient as the linearly polarized light rotates.

- **Crystal cut perpendicular to [111] direction, linearly polarized light**: This

orientation is shown in figure 4.5 (c) and one can show that [2]:

$$\hat{p} = \left(\frac{\cos\theta}{\sqrt{2}} + \frac{\sin\theta}{\sqrt{6}}\right)\hat{x} + \left(\frac{\sin\theta}{\sqrt{6}} - \frac{\cos\theta}{\sqrt{2}}\right)\hat{y} - \frac{2\sin\theta}{\sqrt{6}}\hat{z} \tag{4.25}$$

By substituting this into the equation we obtain the TPA coefficient:

$$\beta = \frac{3\omega}{2\epsilon_0 n^2 c^2}\mathsf{Im}(\chi_{1111})\left(1 - \frac{\sigma}{2}\right) \tag{4.26}$$

that shows no change when the polarization is rotated.

Comparing the results from the experiment on linearly polarized light with what we summarized above about the anisotropic and isotropic media we have two possibilities:

1. Silicon used in this detector has a very low anisotropy factor σ. If this assumption is correct then with any crystal cut for the silicon layer inside the detector we don't see a significant change in the TPA coefficient.

2. Silicon used in the detector is cut perpendicular to the [111] direction which according to Eq. 4.26 does not have any angular dependence.

In order to have a better comparison we can consider the circularly polarized light and compare the theoretical results of the isotropic and the (111) crystal. For the crystal cut perpendicular to the [111] direction it is more complicated to analyze the circularly polarized light. We can analyze the elliptically polarized light by assuming imaginary and real

parts for the unit vector $\hat{p}$ by defining two vectors $\hat{p}_1$ and $\hat{p}_2$ such that:

$$\begin{aligned} \hat{p} &= \hat{p}_1 + j\hat{p}_2 \\ \hat{\eta} \times \hat{p}_1 &= \hat{p}_2 \\ |\hat{p}_1|^2 + |\hat{p}_2|^2 &= 1 \end{aligned} \tag{4.27}$$

Choosing $\hat{p}_1$ and $\hat{p}_2$ of the following form satisfies the conditions in Eq. 4.27:

$$\begin{aligned} \hat{p}_1 &= r\left[\left(\frac{\cos\theta}{\sqrt{2}} + \frac{\sin\theta}{\sqrt{6}}\right)\hat{x} + \left(\frac{\sin\theta}{\sqrt{6}} - \frac{\cos\theta}{\sqrt{2}}\right)\hat{y} - \frac{2\sin\theta}{\sqrt{6}}\hat{z}\right] \\ \hat{p}_2 &= \sqrt{1-r^2}\left[\left(\frac{\cos\theta}{\sqrt{6}} - \frac{\sin\theta}{\sqrt{2}}\right)\hat{x} + \left(\frac{\sin\theta}{\sqrt{2}} + \frac{\cos\theta}{\sqrt{6}}\right)\hat{y} - \frac{2\cos\theta}{\sqrt{6}}\hat{z}\right] \end{aligned} \tag{4.28}$$

where $-\frac{1}{\sqrt{2}} \leq r \leq \frac{1}{\sqrt{2}}$ is a factor that determines the degree of ellipticity of the polarization state. If $r = 0$ the light is linearly polarized and when $r = \pm\frac{1}{\sqrt{2}}$ the light is circularly (left-hand or right-hand) polarized. The angle θ in this case is the angle between the ellipse symmetric axis and $[1\bar{1}0]$ axis of the crystal. After calculating $\hat{p}$ from Eq. 4.28 and substituting in Eq. 4.19 we can show that:

1. The two-photon absorption coefficient β does not depend on the angle θ.

2. β depends on r (the degree of ellipticity of the polarization state):

$$\beta = \frac{3\omega}{2\epsilon_0 n^2 c^2}\left[2\mathsf{Im}(\chi_{1212}) + \left(1-2r^2\right)^2\mathsf{Im}(\chi_{1221}) + \sigma\mathsf{Im}(\chi_{1111})\left(\frac{1}{2} - \frac{2r^2(1-r^2)}{3}\right)\right] \tag{4.29}$$

If we assume that $\chi_{1221} = \chi_{1212}$ then we can simplify this equation in the following

form [2]:

$$\beta = \frac{3\omega}{2\epsilon_0 n^2 c^2}\mathsf{Im}(\chi_{1111})\left[\frac{1}{3}(1-\sigma)\left(2+\left(1-2r^2\right)^2\right)+\sigma\left(\frac{1}{2}-\frac{2r^2(1-r^2)}{3}\right)\right] \tag{4.30}$$

which can be written as a function of the angle γ in the Poincare sphere (figure 4.4) using the relationship $r = \sin\left(\frac{\pi}{4}-\frac{\gamma}{2}\right)$:

$$\beta = \frac{3\omega}{2\epsilon_0 n^2 c^2}\mathsf{Im}(\chi_{1111})\left(1-\frac{\sigma}{2}\right)\left(\frac{5-\cos(2\gamma)}{6}\right) \tag{4.31}$$

which is similar to Eq. 4.13 derived for an isotropic material.

3. By substituting $r = 0$ ($\cos(2\gamma) = -1$) for linearly polarized light and $|r| = \frac{1}{\sqrt{2}}$ ($\cos(2\gamma) = 1$) for circularly polarized light we can show that:

$$\frac{\beta_{\text{lin}}}{\beta_{\text{cir}}} = \frac{3}{2} \tag{4.32}$$

which is the same result as what we found for the isotropic material.

Eq. 4.32 shows that the behavior of a crystal cut perpendicular to [111] for the circularly polarizes light is similar to the experimental results for the silicon detector. Since we do not have any information about the anisotropy factor for silicon and susceptibility elements it is hard to determine whether silicon is behaving as an isotropic material or it has a (111) crystal cut.

[2] The assumption that$\chi_{1221} = \chi_{1212}$ is confirmed experimentally for GaAs and CdTe [2].

5. COMPARISON WITH ANOTHER APD

In this chapter we compare the results from the Silicon APD used in our experiments (detector A) with the TPA response of another silicon APD (detector B). The three specific experiments that we consider in this comparison are:

- Plotting the TPA photocurrent (or voltage) vs. optical power and comparing the regions for which the two detectors show a good TPA response.
- Plotting the spot-size response with the same method explained in Section 3.6.
- Measuring the TPA response in one of the transverse directions of the detector and comparing the degree of uniformity.

The experimental setup used in this chapter is the same as the one used in previous chapter. The detector used in this part comes with a preamplifier circuit and the part number is given in Appendix A.

5.1 TPA Response of the Detector

The output voltage of the lock-in detector is plotted vs. the optical power and the voltage and power are measured as explained is Section 3.2. The curves corresponding to the response of each detector is given in figures (a) and (b). The most important observations are:

1. Detector A saturates at high optical powers whereas detector B does not show any saturation in high optical powers.

2. Detector B shows single-photon (linear) absorption in low powers whereas detector A does not show any linear absorption in low powers.

3. The useful range of the input optical power for each detector to get a TPA response without saturation or linear absorption is shown in table 5.1. It is important to mention that the upper power limit for detector B is determined by the maximum power from the EDFA that can be focused on the detector. Also the lower power limit for detector A is determined by the noise level and is the lower power that the lock-in amplifier can detect.

Detector	Optical Power Range	Output Voltage Range
A	$0.2\,\mathrm{mW} < P < 10\,\mathrm{mW}$	$0.01\,\mathrm{mV} < V_{LIA} < 10\,\mathrm{mV}$
B	$5\,\mathrm{mW} < P < 50\,\mathrm{mW}$	$0.3\,\mathrm{mV} < V_{LIA} < 300\,\mathrm{mV}$

Tab. 5.1: Comparison between the useful ranges of two APD detectors.

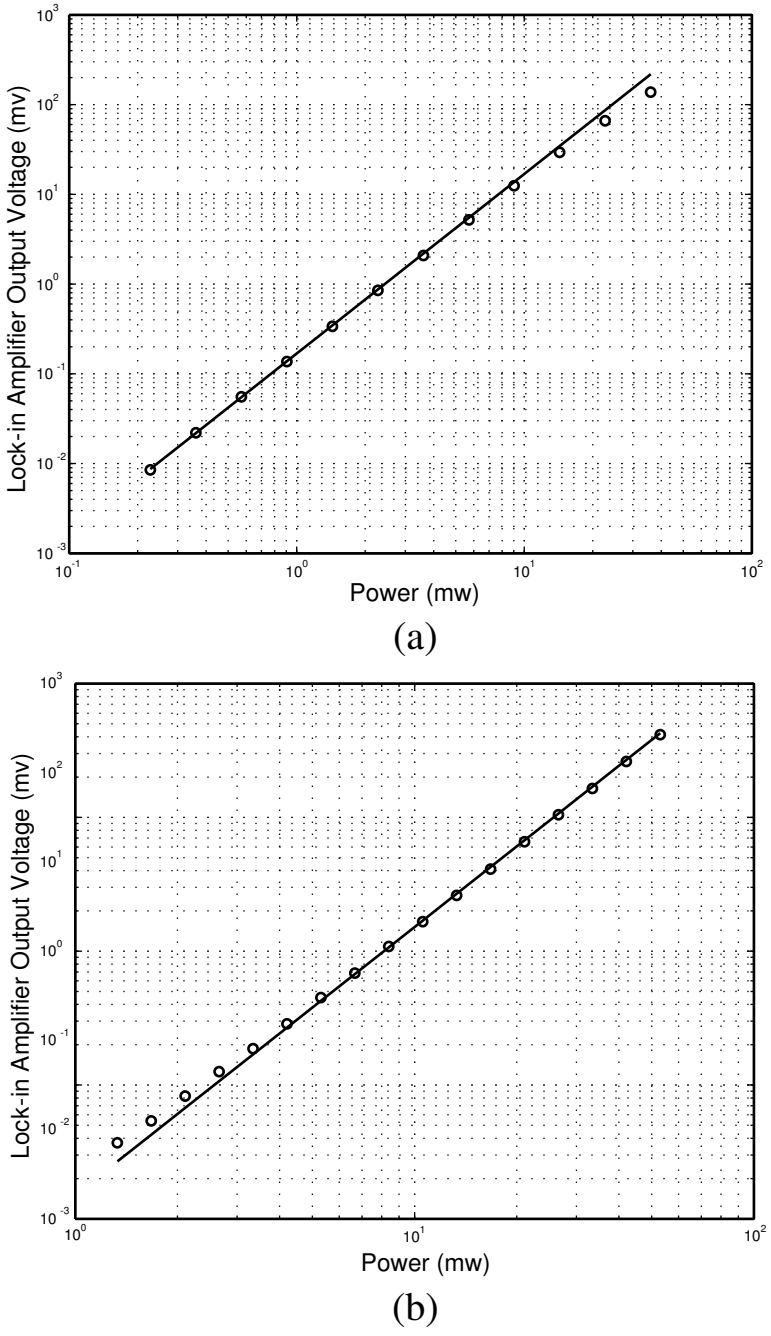

Fig. 5.1: Comparison between the TPA response of detector A (a) and detector B (b). The straight line shows the ideal TPA process (figs/5/tpa-comp.eps)

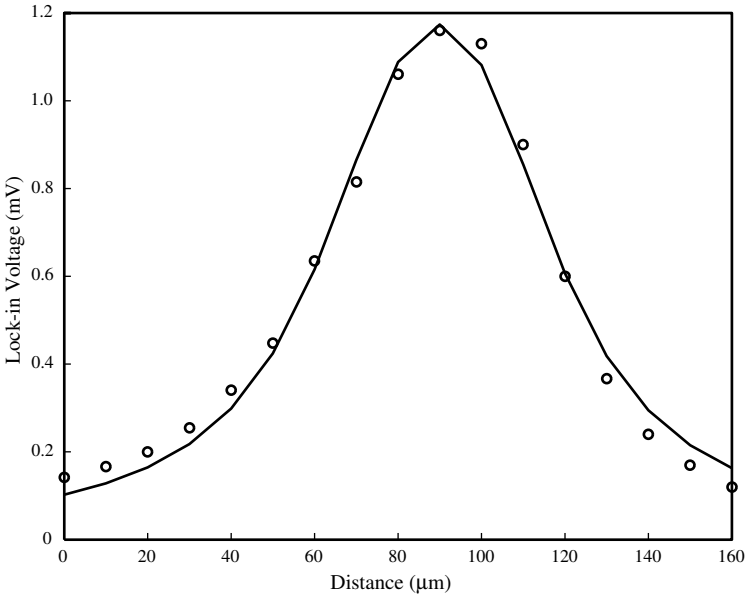

Fig. 5.2: The spot-size sensitivity of the TPA process in detector B using 10× lens.
(figs/5/spotsize-new.eps)

5.2 Spot-size Sensitivity

In this section we repeat the experiment explained in 3.6 with detector B. The 10× lens in used to focus the light on the detector. The curve showing the variation of the TPA output voltage vs. distance in the z direction is given in figure 5.2. With the fitting program explained in Section 3.6 we calculated the spot-size and the effective thickness of detector B (this is the effective thickness because of the interference effect explained in Section 3.8.2). The effective thickness of the layer found by this method is about 130 μm and the spot-size calculated from the fitting program is about 3.5 μm which is close to the real spot-size of this lens.

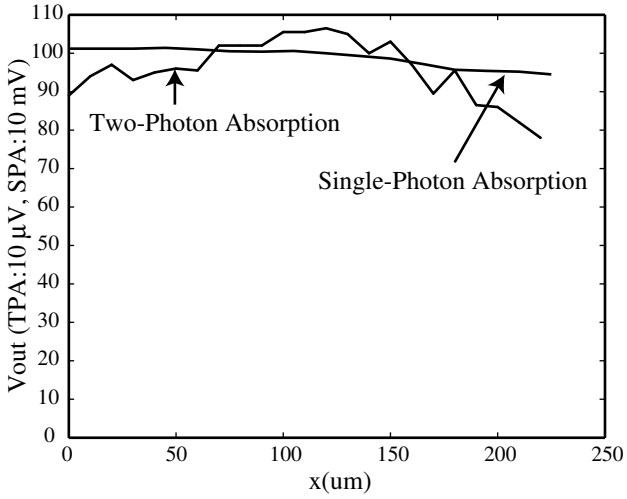

Fig. 5.3: The TPA and SPA voltages vs. transverse location of the beam on the detector. (figs/5/trans-new.eps)

5.3 Uniformity of the Surface

The nonuniform response of detector A was discussed in Section 3.8 and we saw a high degree of nonuniformity caused by a complex interference effect in the detector. Now we do the same measurement to see if this detector has the same response. Detector B has a wider active area of 1.5 mm diameter. In order to scan one complete diameter of the detector with our translation stage we need to divide the path into 7 pieces. Therefore we found an area around the center of the detector and measured the linear absorption and the TPA as we moved the detector by 200 μm which is the maximum range of the fine movement of the stage. The response for the two absorption processes is plotted in figure 5.3 vs. position. For detector B we can also see some nonuniformity for the TPA that

distinguishes between the linear absorption (flat response) and the two-photon absorption. But if we look at figure 3.11 we see much more nonuniformity for detector A. This could be due to a greater parallelism between the front and back surfaces in detector B or lack of a reflective surface on the back surface of detector B. The uniformity of the TPA response is very important because a nonuniform response makes it harder to align the system. In order to build a system for optical communication purposes it is important to make the system insensitive to the alignment.

5.4 Conclusion

We did not have the opportunity to do measurements on the polarization sensitivity and wavelength dependence of detector B. Comparing the measurements on the two detectors we can summarize the conclusion as follows:

1. Two major processes limit the TPA process from the two sides. At low powers the residual single-photon absorption becomes dominant and at high powers saturation occurs.

2. Depending on the detector, the range of the input power needed to observe the TPA process can be different. In this case we compared two Silicon avalanche photodiodes (Si-APD) and the ranges were quite different even though the focusing conditions were identical. In other research, people have used different detectors such as different types of laser diodes, waveguides and LEDs. There is a variety of power

ranges to observe TPA process depending on the type of the detector.

3. The TPA response of the detectors when the beam is moved in the transverse plane was different. Detector B exhibits much less nonuniformity and one future research direction can be working on different fabrication processes or designs that can give the least possible nonuniformity.

6. CONCLUSION

In this thesis, different factors affecting the TPA in a Si-APD detector were investigated. Based on these factors we discussed different considerations in the fabrication of a customized detector for TPA. The thickness of the absorption layer inside the detector, shape and smoothness of the metal contacts, design of the antireflection coating are some of these fabrication issues that we considered.

As we showed in the first part of Chapter 3, a measurable two-photon absorption photocurrent may be observed even for a CW light source. Also we described some experimental considerations to see the TPA with the CW source. By fabricating customized TPA detectors one could even achieve a better response for the TPA for a wider range of the optical input power.

TPA is a process that is sensitive to localization in the time and space domains. We discussed the spot-size sensitivity which is the localization in space. Also in the applications of TPA, we mentioned autocorrelation and cross-correlation methods that are based on the sensitivity of TPA process to localization in time. A cross-correlation system can also be considered as a phase detection system that shows the amount of time delay between two

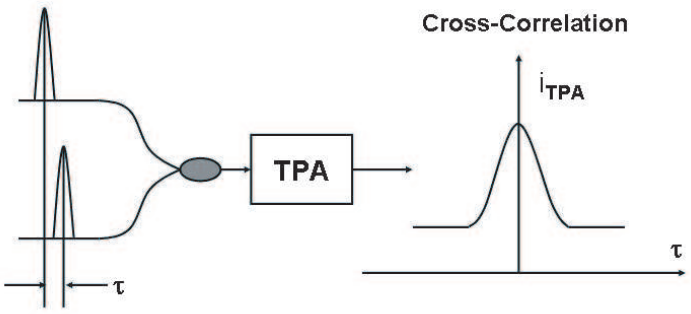

Fig. 6.1: Phase-detection system based on TPA. The delay between the two pulses changes the TPA photocurrent (figs/6/phase-detection.eps)

optical pulses. This gives us ideas for the future work in this research in utilizing the TPA process for a fast clock-recovery system.

6.1 Clock Recovery System based on TPA

One of the most critical components of a clock recovery system is the phase detection, which determines the relative timing difference between a data sequence and a locally generated pulse. Figure 6.1 shows how a TPA detector can operate as a phase detection system. The delay between two pulses that are incident on the detector determines the amount of the photocurrent. There is a peak in the TPA photocurrent when the delay

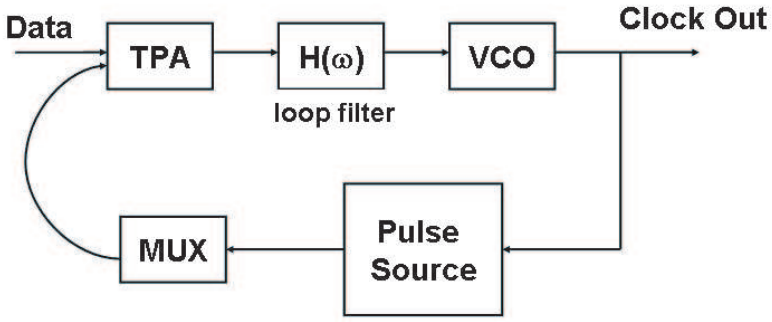

Fig. 6.2: Block diagram of a clock-recovery system based on TPA (figs/6/clock-recovery.eps)

between the pulses is zero. The photocurrent vs. time delay between pulses is shown in figure 6.1. A nonlinear detector can be used as a phase detection system, whereas a linear detector would give the same average photocurrent regardless of the relative timing. Figure 6.2 shows the block diagram of the clock-recovery system proposed. This system has several advantages compared with other methods of clock-recovery:

- **Ultrafast response time**: The TPA process is a fast process, meaning that the localization of power in time is detectable with a very short response time. Therefore the electronics in the system need only be fast enough to detect changes in the average photocurrent. This is the main advantages of this process which makes it suitable for an ultrafast clock-recovery system.

- **Large bandwidth**: The TPA in a silicon detector can be observed for a wide range of optical frequencies:

$$\frac{E_g}{2h} \leq \nu \leq \frac{E_g}{h} \tag{6.1}$$

- **Less polarization sensitive**: The TPA process has some polarization dependence as we discussed in Chapter 4 but this dependence is still weaker than many other methods used for clock-recovery systems.

- **No phase matching**: In systems working with the second-order nonlinearity ($\chi^{(2)}$), phase matching is required, but in a TPA-based system phase matching is not required.

- **High sensitivity (low power)**: The system can operate with low levels of optical powers that we measured in Section 3.2.

- **Possible to use for high duty cycle RZ signals**: High duty cycle signals are very close to CW light and we showed that it is possible to observe TPA with CW light.

One future direction of this research will be developing a clock-recovery system using the nonlinear TPA detector described in this work.

APPENDIX

A. TECHNICAL DATA ON THE EXPERIMENTAL SETUP

In this appendix we give some technical information on the parts used in our experimental setup. Most of the parts explained below are shown in the schematic of the setup in figure 3.1.

- **Laser**: Agilent 81682A tunable laser. The wavelength is set to 1550 nm in most of the experiments and is tuned in a range of $\pm$20 nm about 1550 nm for those measurements involving wavelength sensitivity. The power of the laser is set to 300 μm (-5 dBm) in all of the experiments.

- **EDFA**: IPG Photonics erbium-doped fiber amplifier model EAD-100-C. The EDFA is set on the power-control mode and set at the maximum power which is about 120 mW.

- **Polarization Controller**: Mechanically controlled polarization controller made by Fiber Control.

- **Optical Tap Coupler**: The couple is a Gould Fiber Optics product and it taps off 5% of the the input power for monitoring.

Diameter	Breakdown Voltage	Spectral Range	Peak Wavelength	Q.E.(900 nm)
500 μm	205 V	400 to 1000 nm	830 nm	60 %

Tab. A.1: Some features of the main detector used in the experimental setup.

- **Power Meter**: HP 81531A power meter module.
- **Variable Attenuator**: JDS Uniphase optical attenuator model HA9. The attenuation is variable from 0 to 100 dB with the steps as low as 0.001 dB.
- **Chopper**: Stanford Research Systems optical chopper model SR540. The frequency of the chopper in all of the experiments was 330 Hz.
- **Filter**: CVI laser long-pass (LP) filter model LPD-1200-1.00. The filter passes wavelengths above 1200 nm and the diameter of the filter is about 1 inch.
- **Microscope Objective**: Both 10X and 20X microscope objectives are Edmund Optics product. The part numbers are NT43-903 and NT38-339 respectively and their technical data are gives in table 3.1
- **Lock-In Amplifier**: EG&G product model 5209.
- **Main Detector**: Silicon Avalanche Photodiode model C30902E made by Perkin Elmer Optoelectronics. Some of the features of this detector are given in table A.1. The avalanche gain of the device depends on the bias voltage and for a bias voltage of 195 V is about 100.

R	R_b	C	OPAMP
200 kΩ	1 MΩ	10 nF	OP27C

Tab. A.2: Numerical values of electronic components used in the circuit shown in figure 3.2.

Diameter	Spectral Range	Peak Wavelength	Q.E. (800nm)	Photosensitivity (V/W)
1.5 mm	400 to 1000 nm	800 nm	78 %	1.5×10^6

Tab. A.3: Some features of the second detector used in chapter 5

- **Amplifier Circuit** In order to convert the photocurrent to voltage we used the circuit given in figure 3.2. Table A.2 shows the numerical values of the components and the type of the Opamp used in this circuit. A metal box contains the circuit and the detector and can be mounted on regular optical table mounts.

- **Second Detector**: The other detector used in the experiment discussed in Chapter 5 is a Silicon avalanche photodiode module made by Hamamatsu. The model number is C5460 and it has a built-in amplifier circuit and high-voltage source. Some features of this module are given in table A.3. The avalanche gain of this detector is also variable and can be adjusted. The preset value of the gain is about 30.

B. GAUSSIAN BEAMS

A thorough analysis of the Gaussian beams is given in [23] and [21]. In this appendix we list some of the formulas we need for the measurements we did in this thesis. Also we solve the problem of a Gaussian beam entering a medium with a different refractive index.

B.1 Formulation of Gaussian Beams

Suppose that we have a medium with refractive index n which is constant in time, uniform in space, and purely real. In this case we can write the well-known Helmholtz Equation:

$$\nabla^2 \mathbf{E} + k^2 \mathbf{E} = 0 \tag{B.1}$$

where $k = \dfrac{n\omega}{c}$ is the wave number. The kind of solution that results in Gaussian beams is that of a nearly plane wave in which the flow of energy is predominantly along the z direction and the electric field is in the transverse direction. If E is one of the transverse

components of $\mathbf{E}$ we can write:

$$E(x, y, z) = \psi(x, y, z)e^{-jkz} \tag{B.2}$$

And by substituting ∇^2 for the cylindrical coordinates and assuming that $\frac{\partial^2\psi}{\partial z^2} \ll k^2\psi$ and $\frac{\partial^2\psi}{\partial z^2} \ll k\frac{\partial\psi}{\partial z}$, we can show:

$$\left(\frac{\partial^2}{\partial r^2} + \frac{1}{r}\frac{\partial}{\partial r}\right)\psi - 2ik\frac{\partial\psi}{\partial z} = 0 \tag{B.3}$$

Solving this equation leads to the following expression for ψ:

$$\psi = \exp\left(-j\left[P(z) + \frac{k}{2q(z)}r^2\right]\right) \tag{B.4}$$

By substituting this expression into Eq. B.3 we can show that:

$$\begin{aligned} q(z) &= q_0 + z = j\frac{\pi w_0^2 n}{\lambda} + z \\ P(z) &= -j\ln\left(1 + \frac{z}{q_0}\right) \end{aligned} \tag{B.5}$$

where w_0 is constant and is called the minimum spot-size of the beam. By some simple math one can show that the electric field component E can be written as:

$$E(x, y, z) = E_0\frac{w_0}{w(z)}\exp\left[-j\left(kz - \eta(z)\right) - r^2\left(\frac{1}{w^2(z)} + \frac{jk}{2R(z)}\right)\right] \tag{B.6}$$

where $w(z)$ is called the spot-size of the beam, $R(z)$ is the radius of curvature of the phase front and $\eta(z)$ is the phase factor of the beam. These parameters can be calculated using the following formulas:

$$\begin{aligned} w^2(z) &= w_0^2\left(1+\frac{z^2}{z_0^2}\right) \\ R(z) &= z\left(1+\frac{z_0^2}{z^2}\right) \\ \eta(z) &= \tan^{-1}\left(\frac{z}{z_0}\right) \end{aligned} \tag{B.7}$$

where $z_0 = \dfrac{\pi w_0^2 n}{\lambda}$ is called the confocal beam parameter. The parameter $q(z)$ can therefore be calculated from:

$$\frac{1}{q(z)} = \frac{1}{R(z)} - j\frac{\lambda}{\pi w_0^2 n} \tag{B.8}$$

If we calculate the intensity of the beam as a function of (r, z) we have:

$$I(r,z) = I_0 \frac{w_0^2}{w^2(z)} \exp\left(\frac{-2r^2}{w^2(z)}\right) \tag{B.9}$$

This equation shows that the intensity of the beam in a plane perpendicular to the z axis is a gaussian function of r. Also if we look at a plane that includes the z axis (figure B.1) the curve indicating a constant intensity of $\dfrac{I_0}{e^2}$ is represented by the following equation:

$$r^2 = w^2(z) = w_0^2\left(1+\frac{z^2}{z_0^2}\right) \tag{B.10}$$

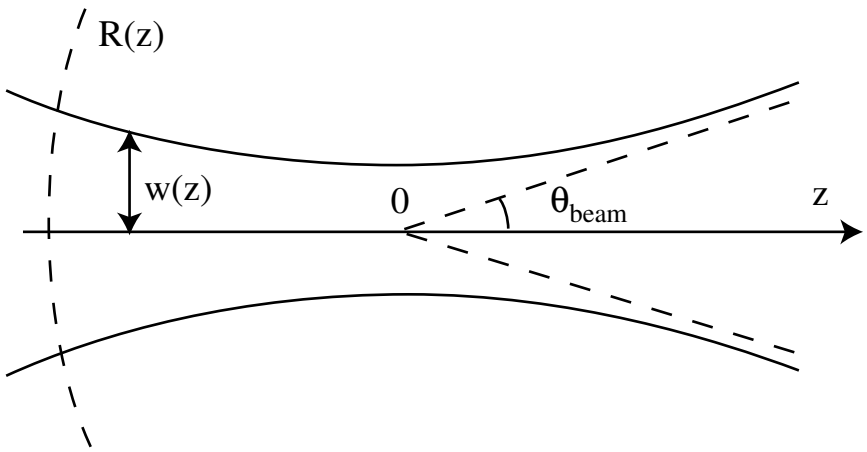

Fig. B.1: Gaussian beam and different parameters. The dashed line shows the divergence angle of the beam at the far field. (figs/B/gaussian-beam.eps)

This equation shows the physical shape of the beam when looked at from the side. It is easy to see that when $z \gg z_0$ (far field) we will get to a line represented by the equation $r = \frac{\lambda}{\pi w_0 n}|z|$ which shows that the angle of diffraction of the beam is:

$$\theta_{\mathrm{beam}} \simeq \frac{\lambda}{\pi w_0 n} \tag{B.11}$$

In figure B.1, this line and the angle of divergence are shown. As seen in the figure and also from Eq. B.7 the spot-size of the beam, $w(z)$ is minimum at $z = 0$ which is called the waist of the beam and the radius of curvature of the phase front, $R(z)$, is infinity at this point.

B.2 Transformation of the Gaussian beam

As we saw before, the parameter $q(z)$ can represent a Gaussian beam since the real and imaginary parts of this parameter give us the radius of curvature and the spot-size of the beam. If a gaussian beam with parameter q_1 enters an optical system with a ray matrix M, the output beam has a parameter q_2 which can be calculated from the following formula [23]:

$$q_2 = \frac{Aq_1 + B}{Cq_1 + D} \quad , \quad M = \begin{pmatrix} A & B \\ C & D \end{pmatrix} \tag{B.12}$$

As an example of such a transformation let us consider the case of a Gaussian beam incident on a thin lens with focal length f such that the waist of the incident beam is on the lens. Figure B.2 (a) shows the Gaussian beam and the lens. w_i is the spot-size of the incident beam and w_f is the spot-size at the focal point which is approximately within a distance f from the lens. Using Eq. B.12 we have:

$$\frac{1}{q_2} = \frac{1}{q_2} - \frac{1}{f} \ , \ M = \begin{pmatrix} 1 & 0 \\ -\frac{1}{f} & 1 \end{pmatrix} \tag{B.13}$$

Considering $n = 1$ for the air and substituting $\frac{1}{q_1} = -j\frac{\lambda}{\pi w_i^2}$ and $q_2 = j\frac{\pi w_f^2}{\lambda} - f$ we can show that:

$$w_f = \frac{\lambda f}{\pi w_i} \tag{B.14}$$

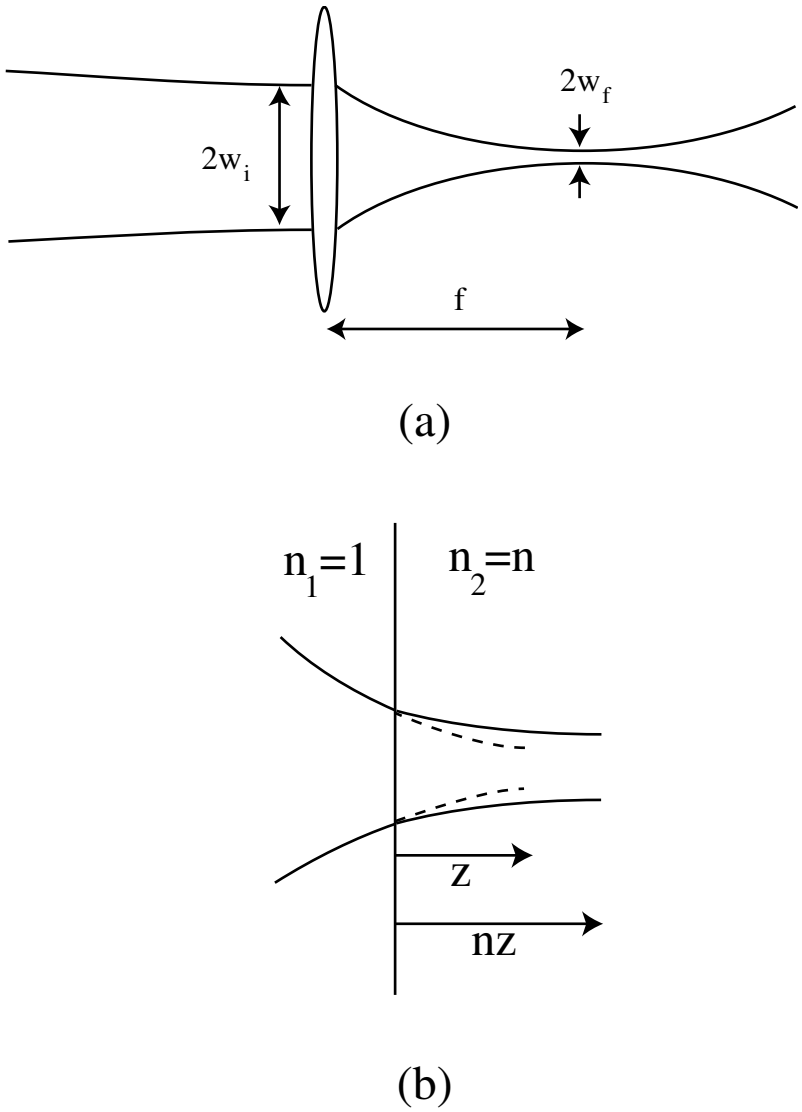

Fig. B.2: Gaussian beam transformation by a thin lens (a) and the refraction of the Gaussian beam (b), the dashed line shows the beam if medium 2 was not present.
(figs/B/trans-gauss.eps)

B.3 Refraction of the Gaussian Beam

Now we utilize the same analysis for the refraction of a Gaussian beam. Suppose that a Gaussian beam with a radius of curvature R_1 and spot-size w_1 is incident from air ($n = 1$) on a transparent material with refractive index n. The radius of curvature and spot-size inside the medium at the boundary are R_2 and w_2 respectively. Using Eq. B.12 for this transformation we have:

$$q_2 = nq_1 \ , \ M = \begin{pmatrix} 1 & 0 \\ 0 & \frac{1}{n} \end{pmatrix} \tag{B.15}$$

By substituting q_1 and q_2 we can write:

$$\frac{1}{R_1} - j\frac{\lambda}{\pi w_1^2} = n\left(\frac{1}{R_2} - j\frac{\lambda}{\pi n w_2^2}\right) \tag{B.16}$$

which gives us the following relationships between Gaussian beam parameters at the two sides of the boundary:

$$R_2 = nR_1 \ \ , \ \ w_2 = w_1 \tag{B.17}$$

These two equations show that:

- The spot-size of the minimum spot-size of the beam inside and outside of the medium are the same.
- The radius of curvature of the beam is multiplied by a factor of n when the beam refracts. It is easy to verify that this is equivalent to multiplying the distance from

the boundary to the focal point by a factor of n. This is shown in figure B.2 (b).

BIBLIOGRAPHY

[1] R. W. Boyd. *Nonlinear Optics*. Academic Press, 1992.

[2] M. D. Dvorak, W. A. Schroeder, D. R. Andersen, and B. S. W. Arthur L. Smirl. Measurement of the anisotropy of two-photon absorption coefficients in zincblende semiconductors. *J. Quantum Electron.*, **30**(2), 256–268, 1994.

[3] J. Gowar. *Optical Communication Systems*. Prentice-Hall International, 1984.

[4] D. Spirit, A. Ellis, and P. Barnsley. Optical time division multiplexing: systems and networks. *IEEE Communication Magazine*, **32**(12), 56–62, 1994.

[5] A. Lattes, H. A. Haus, F. J. Leonberger, and E. P. Ippen. An ultrafast all-optical gate. *J. Quantum Electron.*, **19**(11), 1718–1723, 1983.

[6] P. Butcher and D. Cotter. *The Elements of Nonlinear Optics*. Cambridge University Press, 1990.

[7] E. Sauter. *Nonlinear Optics*. John Wiley and Sons, 1996.

[8] G. S. He and S. H. Liu. *Physics of Nonlinear Optics*. World Scientific, 1999.

[9] A. Yariv. *Quantum Electronics*. John Wiely and Sons, 3rd edition, 1989.

[10] J. K. Ranka, A. L. Gaeta, A. Baltuska, M. S. Pshenichnikov, and D. A. Wiersma. Autocorrelation measurement of 6-fs pulses based on the two-photon-induced photocurrent in a GaAsP photodiode. *Optics Lett.*, **22**(17), 1344–1346, 1997.

[11] K. Kikuchi. Highly sensitive interferometric autocorrelator using Si avalanche photodiode as two-photon absorber. *Electron. Lett.*, **34**(1), 123–125, 1998.

[12] K. Kikuchi, F. Futami, and K. Katoh. Highly sensitive and compact cross-correlator for measurement of picosecond pulse transmission characteristics at 1550 nm using two-photon absorption in Si avalanche photodiode. *Electron. Lett.*, **34**(22), 2161–2162, 1998.

[13] B. Thomsen, L. Barry, J. Dudley, and J. Harvey. Ultra Highspeed all-optical demultiplexing based on two-photon absorption in a laser diode. *Electron. Lett.*, **34**(19), 1871 – 1872, 1998.

[14] B. Thomsen, L. Barry, J. Dudley, and J. Harvey. Ultrafast all-optical sampling at 1.5 μm using waveguide two-photon absorption. *Electron. Lett.*, **35**(17), 1483–1484, 1999.

[15] Z. Zheng, A. Weiner, J. Marsh, and M. Karkhanehchi. Ultrafast optical thresholding based on two-photon absorption GaAs waveguide photodetectors. *IEEE Photon. Technol. Lett.*, **9**(4), 493–495, 1997.

[16] T. Inui, K. Tamura, K. Mori, and T. Morioka. Bit rate flexible chirp measurement technique using two-photon absorption. *Electron. Lett.*, **38**(23), 1459–1460, 2002.

[17] H. Cao, A. Dogariu, W. Warren, and L. Wang. Reduction of optical intensity noise by means of two-photon absorption. *J. Opt. Soc. America B*, **20**(3), 560–563, 2003.

[18] P. G. Chua, Y. Tanaka, M. Takeda, and T. Kurokawa. Infra-red image detection with Si-CCD image sensor due to the two-photon absorption process. *Confrence on Lasers and Electro-Optics*, **1**, I–482–I–483, 2001.

[19] R. A. Negres, J. M. Hales, A. Kobyakov, D. J. Hagan, and E. W. V. Stryland. Experiment and analysis of two-photon absorption spectroscopy using a white-light continuum probe. **38**(9), 1205–1216, 2002.

[20] Y. Tanaka, P. G. Chua, T. Kurokawa, H. Tsuda, M. Naganuma, and M. Takeda. Reflectometry based on two-photon absorption of a silicon avalanche photodiode. In *Optical Fiber Sensors Conference Technical Digest*, volume 1, pages 577–580. 2002.

[21] C. C. Davis. *Lasers and Electro-Optics*. Cambridge University Press, 1996.

[22] G. P. Agrawal. *Nonlinear Fiber Optics*. Academic Press, 3rd edition, 2001.

[23] A. Yariv. *Optical Electronics in Modern Communications*. Oxford University Press, 5th edition, 1996.